# A MICRO-PULSED LIDAR FOR THE STUDY OF THE LOWER TROPOSPHERE AND ATMOSPHERIC BOUNDARY LAYER

by

Erin Michelle Casey

A thesis submitted in partial fulfillment
of the requirements for the degree

of

Master of Science

in

Physics

MONTANA STATE UNIVERSITY
Bozeman, Montana

July 2012

# APPROVAL

of a thesis submitted by

Erin Michelle Casey

This thesis has been read by each member of the thesis committee and has been found to be satisfactory regarding content, English usage, format, citation, bibliographic style, and consistency and is ready for submission to The Graduate School.

Dr. John L Carlsten

Approved for the Department of Physics

Dr. Richard Smith

Approved for The Graduate School

Dr. Carl A. Fox

# STATEMENT OF PERMISSION TO USE

In presenting this thesis in partial fulfillment of the requirements for a master's degree at Montana State University, I agree that the Library shall make it available to borrowers under rules of the Library.

If I have indicated my intention to copyright this thesis by including a copyright notice page, copying is allowable only for scholarly purposes, consistent with "fair use" as prescribed in the U.S. Copyright Law. Requests for permission for extended quotation from or reproduction of this thesis in whole or in parts may be granted only by the copyright holder.

Erin Michelle Casey

July 2012

# DEDICATION

I dedicate this thesis to my family; my parents, Terrance and Lori, my sister Sara, and my brother Donovan. You have been there for me in so many ways, dispelling the darkness, brightening my wanderings, and helping me keep my own candle lit. Thank you for your support, unfailing love, and constant light in my life.

# ACKNOWLEDGEMENTS

I would like to thank my advisors both Dr. John Carlsten and Dr. Kevin Repasky for their assistance and encouragement throughout the process of this project. The time they spent working with me the last three years has been very valuable to me and I appreciate all of it.

The assistance of my group members was always gratefully welcome also. Amin Nehrir, David Hoffman, Will Johnson, and Caleb Stoltzfus were particularly helpful in many ways including discussing ideas, helping me code, and lifting heavy things.

In addition I would like to thank Kevin Repasky and Joe Shaw and their staff for establishing and maintaining the Bozeman, Montana, AERONET site used in this work. I would also like to thank Joe Shaw for the use of the weather station data used in the case studies. The Calipso satellite data presented in this thesis was obtained from the NASA Langley Research Center Atmospheric Science Data Center.

TABLE OF CONTENTS

TABLE OF CONTENTS – CONTINUED

# LIST OF TABLES

Table Page

# LIST OF FIGURES

Figure Page

LIST OF FIGURES-CONTINUED

Figure Page

LIST OF FIGURES-CONTINUED

Figure Page

# ABSTRACT

The current largest unknown variable in global climate models is the effect of aerosols directly and indirectly on radiative forcing. This thesis continues the work of characterizing this effect through the study of aerosols by the use of lidar. A micro-pulsed lidar was designed, fabricated and incorporated into a set of instruments for atmospheric studies at Montana State University. The data collected up to this point shows the usefulness of employing such a system in conjunction with other remote sensing instruments as well as in-situ instruments. This is shown by the retrieval of aerosol backscatter and extinction coefficients as well as lapse rates and atmospheric boundary layer heights.

# CHAPTER ONE – ATMOSPHERIC STUDIES

## Atmosphere Structure

### Introduction

The micro-pulsed lidar is being developed to complement a set of remote sensing and in-situ instruments developed and deployed at Montana State University for the purpose of atmospheric studies. As a starting point, a brief overview of the atmospheric structure will be presented. As seen in Figure (1) there are four layers distinguished by their temperature gradient corresponding to various heights. The troposphere can be further divided into the region just above the Earth's surface known as the Atmospheric Boundary Layer and the region above the Atmospheric Boundary Layer known as the free troposphere. The troposphere plays an important role in both weather and climate and observational tools and data retrievals are necessary.

### The Atmospheric Boundary Layer

The Atmospheric Boundary Layer (ABL) is created by a capping temperature inversion which traps moisture, pollutants, and aerosols. This capping inversion, due to density and buoyancy, maintains a separation of the ABL and the free troposphere. Though the ABL is roughly stable it does undergo daily changes due to both thermal mixing from solar radiation, as well as exchanges with the free troposphere. As Figure (2) depicts solar radiation heating the ground creates thermals that rise and effectively mix the ABL. At nightfall this mixing ceases and the cooling ground creates a stable boundary layer.

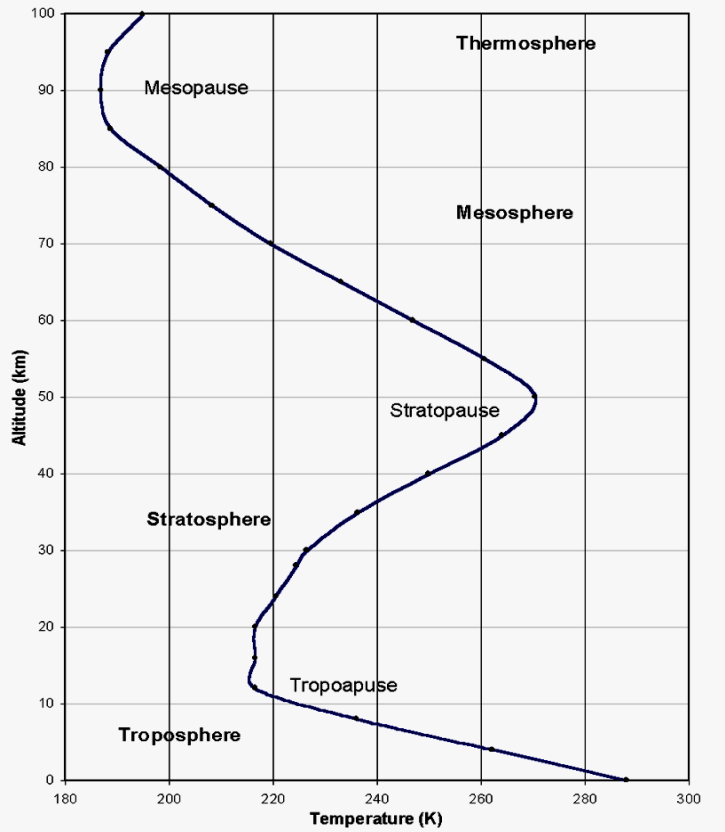


Figure (1) The regions of the atmosphere as characterized by their temperature gradient due to height (US Standard Atmosphere [1]).

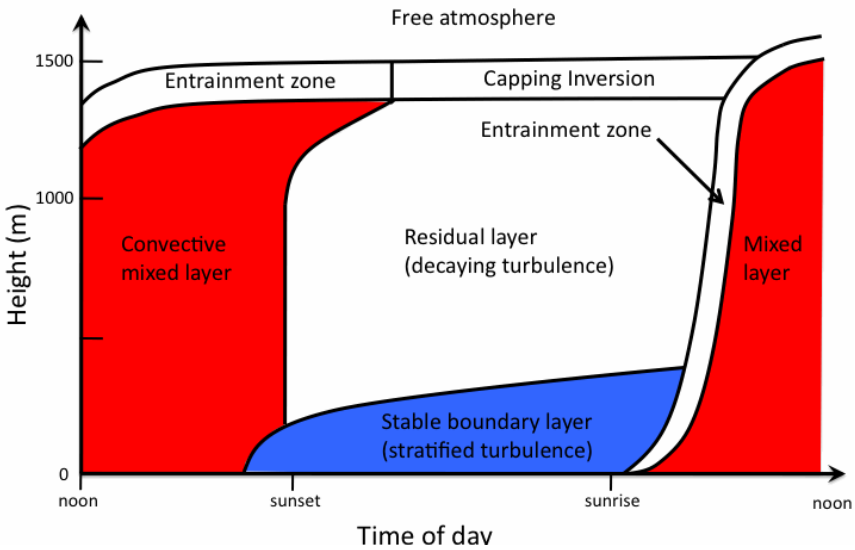


Figure (2) ABL evolution through 24 hr. (adapted from Stull [2]). At sunset the mixed layer settles into a stable boundary layer and a residual layer as the ground cools and heating ceases. At sunrise the heating of the ground creates thermals that mix this layer. The Entrainment zone allows for partial mixing with the free troposphere.

As seen in Figure (2) any alteration in the solar radiation reaching the Earth's surface will affect the evolution of the boundary layer. Aerosols can reduce and redistribute this radiation through scattering and suppress the growth of the ABL. However, as discussed by Yu et al. [3], absorbing aerosols will heat the atmosphere and increase the growth of the ABL. Thus looking at the evolution of the ABL will provide a characterization of the aerosols contained therein.

As might be assumed from the many differing physical properties between the ABL and the free troposphere the gradient in temperature due to height, known as the lapse rate, is not always a constant as it is depicted in Figure (1). When the lapse rate at the top of the ABL is opposite that of the free troposphere and lower ABL it is termed an inversion. In the inverted region the temperature will increase through to the free troposphere and then begin to decrease again. Though inversions are common in Bozeman, Montana, the correction is minimal and the assumption that the lapse rate is a constant for the entirety of the troposphere has been shown to be valid by Rennick's work [4]. As such, a negative constant lapse rate will be used in this work.

## Radiative Forcing

Changes in the troposphere and specifically in the ABL, can be illuminated by the global energy balance. As seen in Figure (3) the global energy balance describes the net flux of energy through the atmosphere. As might be expected, conservation of energy requires that the net flux is always 0. An instantaneous change in the net downward flux density at the top of the atmosphere is termed radiative forcing and labeled $F$. A gradual

change in the temperature of the surface air, $T_s$, will re-balance the global energy. The change of the surface temperature due to all radiative forcing factors is known as the climate sensitivity, $\lambda$, which Wallace and Hobbes [5] defined as

$$\lambda = \frac{dT_s}{dF} = \frac{\partial T_s}{\partial F} + \sum_i \frac{\partial T_s}{\partial y_i}\frac{dy_i}{dF}. \quad \{1\}$$

The climate sensitivity is the total derivative of temperature and is dependent on any additional factors, $y_i$, that are affected by radiative forcing as well. These factors include, but are not exclusively, atmospheric water vapor, low clouds, and cloud albedo.

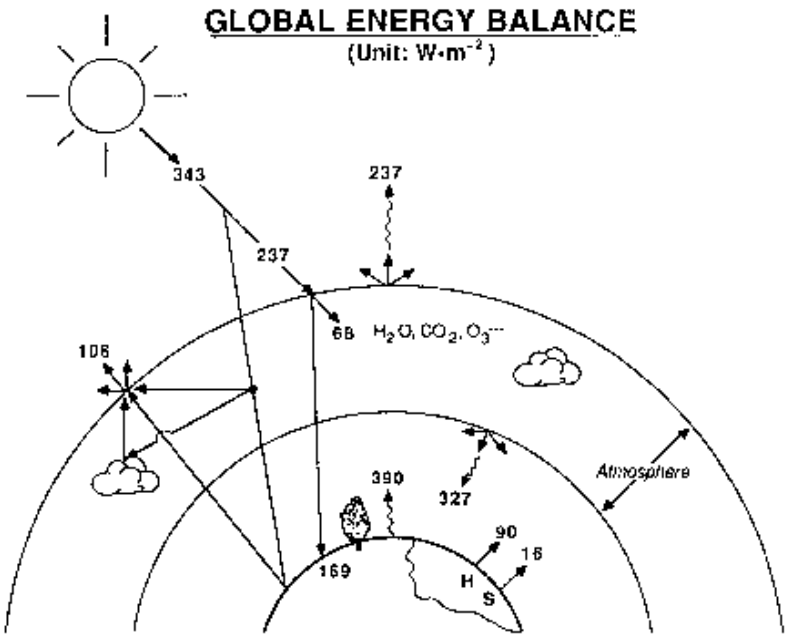


Figure (3) The Global Energy Balance (Morcrette [6]). The solar radiation of typical 343 W/m$^2$, is incident on the atmosphere. It is scattered, absorbed, and radiated to create a 0 net energy flux.

Since it can take the troposphere decades to thermally equilibrate, versus months for the stratosphere, radiative forcing is generally taken as the flux through the

tropopause. This difference in rate of equilibration is due largely to the thermal inertia of the oceans and the fact that the stratosphere is decoupled from this underlying media. These decade long readjustments for the troposphere contribute to climate change, which is defined as the change in average surface temperature.

Wallace and Hobbes [5] show the usefulness of defining the feedback factors, $f_i$, which describe the interdependence of temperature and the above mentioned factors

$$f_i = \frac{\partial T_s}{\partial y_i}\frac{dy_i}{dT_s}. \quad \{2\}$$

The climate sensitivity can then be written as

$$\lambda = \frac{\partial T_s}{\partial F} + \sum_i \frac{\partial T_s}{\partial y_i}\frac{dy_i}{dT_s}\frac{dT_s}{dF} = \frac{\partial T_s}{\partial F} + \frac{dT_s}{dF}\sum_i f_i. \quad \{3\}$$

Note that the $f_i$'s can be positive or negative as can the direct dependence of the temperature on the forcing factor. Thus while the direct dependence might indicate a positive temperature change the feedback factors could in-fact create a negative forcing; resulting in a temperature drop.

## Aerosol Effect on Radiative Forcing

Aerosols will affect the forcing of the atmosphere. Coakley and Chylek [7] found from a theoretical basis that this "heating effect" is dependent on the ratio of absorption to backscatter cross-section. Chylek and Wong [8] later found the direct radiative forcing of soot to be between -.2 and -1.1 W/m$^2$ dependent on the size of the aerosol. Haywood and Shine [9] did similar theoretical work on soot and determined a direct radiative forcing of +0.03 to +0.24 W/m$^2$. Through this theoretical work how aerosols are

involved in determining the climate is seen. However, as might be evident in this wide variation of results, the Intergovernmental Panel on Climate Change (IPCC) report issued in 2007 [10] indicated that anthropogenic aerosols in total had a direct radiative forcing between -0.5 and +0.4 $W/m^2$.

Aside from the direct effect aerosols have on radiative forcing they also influence other physical factors and have an indirect effect. Aerosols have a great indirect effect on radiative forcing through the cloud albedo or reflectivity, as argued by Twomey [11], and as such, this has been defined as the first indirect effect of aerosols. It is this indirect effect that is listed by the IPCC as the largest unknown in radiative forcing models of climate change. McComiskey et al. [12] in particular have characterized the error in finding the relationship between cloud albedo interacting with aerosols and radiative forcing. However, the IPCC still reports an estimate of -0.7 $W/m^2$ with a variation of -1.8 to -0.3 $W/m^2$ for the radiative forcing due to this indirect effect of aerosols through cloud albedo. Thus, while there has been much work devoted to this area of study there is still a need for a more precise description of aerosol influence on radiative forcing both directly and indirectly.

## Lidar Basics

Lidar, LIght Detection And Ranging, uses highly time sensitive components to determine the time difference between a transmitted beam and detection of the backscattered beam. Pulsed lasers are used to create high powered signals and well-defined timing of transmission. The physical process is that of radar: the signal is

transmitted, it hits an object at a distance creating a scattered field and the portion scattered directly back is detected. This process is illustrated in Figure (4). After careful analysis of the returned light, this will yield information about the scattered and absorbed portion of the beam. As this will be proportional to the density of scatterers, lidar has become a preferred method for studying aerosols, trace gases, and atmospheric pollutants.

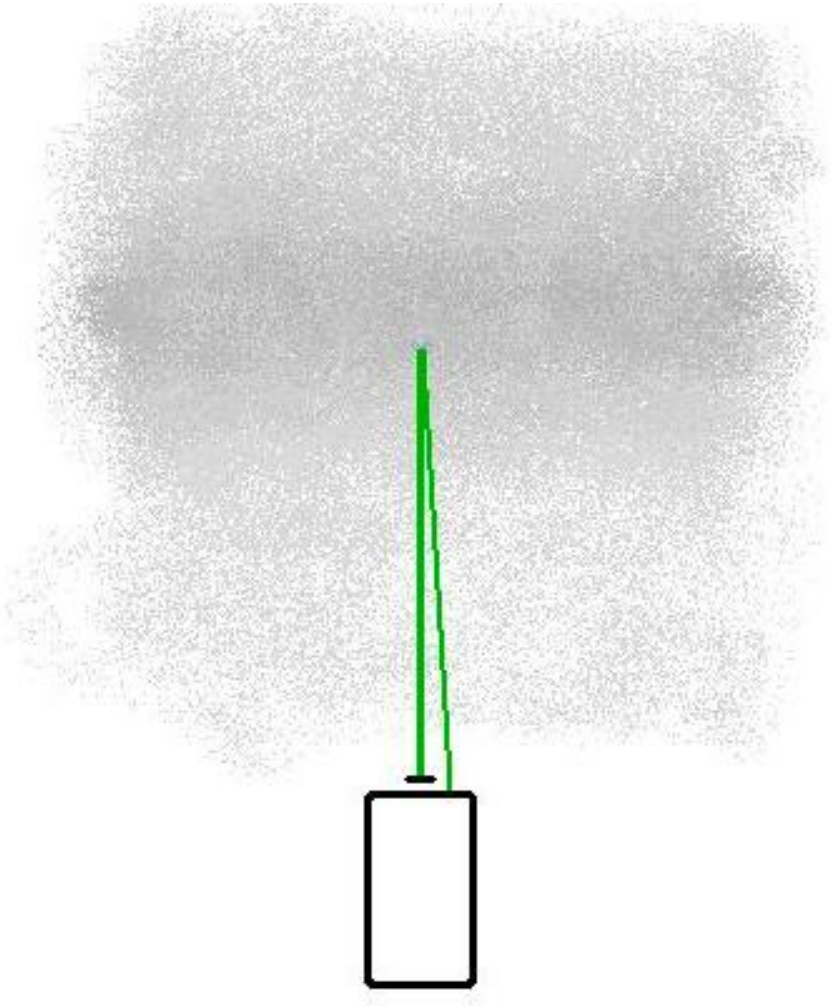

Figure (4) The 532 nm green laser is transmitted from the obscuration of a telescope to the aerosol filled ABL. It is scattered by a particle or molecule and the portion scattered in the direction of the telescope is detected. The distance to the scatterer can be derived by using the speed of light and the time for the round trip: $2r = ct$.

## Contained in this Thesis

In this thesis the micro-pulsed lidar (MPL) is described in chapter two along with constraints that were considered in its design. Chapter three details the retrieval of backscattering and extinction coefficients from the returned intensity through the inversion process. Chapter four contains studies performed using the micro-pulsed lidar of the troposphere above Bozeman, Montana. Chapter five contains conclusions based upon the studies presented in chapter four and future work to be done with the micro-pulsed lidar.

# CHAPTER TWO – INSTRUMENT DESIGN

## Design of the Micro-Pulsed Lidar Instrument

A schematic of the micro-pulse lidar described in the thesis is shown in Figure (5). The laser source is a Teem Photonics Nd:YAG frequency doubled 532 nm passively Q-switched laser that operates with an estimated pulse repetition frequency (PRF) of 7.2 kHz, a nominal pulse energy of 3 μJ and a pulse duration of less than 1 ns. The light exiting the laser is incident on a Half-Wave-Plate ($\lambda / 2$) and polarizing beam splitter (PBS). The light passing through the PBS is incident on a photodiode used to trigger the data acquisition while the light rejected by the PBS is sent to a beam expander. The Half-Wave-Plate allows adjustment of the ratio of light that passes through and is rejected by the PBS. The light rejected by the PBS is expanded using a Thorlabs BE10M-A beam expander. This light is collimated and is incident on the turning mirrors that allow the light to be sent into the atmosphere using a co-linear lidar configuration. Table (1) lists the lidar laser transmitter parameters.

Light scattered in the atmosphere is collected using a Schmidt-Cassegrain telescope with a 278 mm diameter and an f-number (ratio of focal length to diameter) of f/10. Light from the telescope passes through a focus and is collimated using a 250 mm focal length lens. The collimated beam with a beam diameter of 25 mm next passes through a narrow band filter with a center wavelength of 532 ± 0.2 nm and a full width half maximum band pass of 1 ± 0.2 nm. This light is next coupled into a 105 μm core diameter fiber using a Thorlabs PAF-X-11-PC-A fiber coupler with an N.A. of 0.5, a

focal length of 11 mm, and a clear aperture of 1.8 mm. This light is then directed via the optical fiber to an avalanche photodiode (APD) operating with an efficiency of 54% at 532 nm, a dark count rate average of 150 Hz and a saturation count rate of 12 MHz. The lidar receiver parameters are summarized in Table (2).

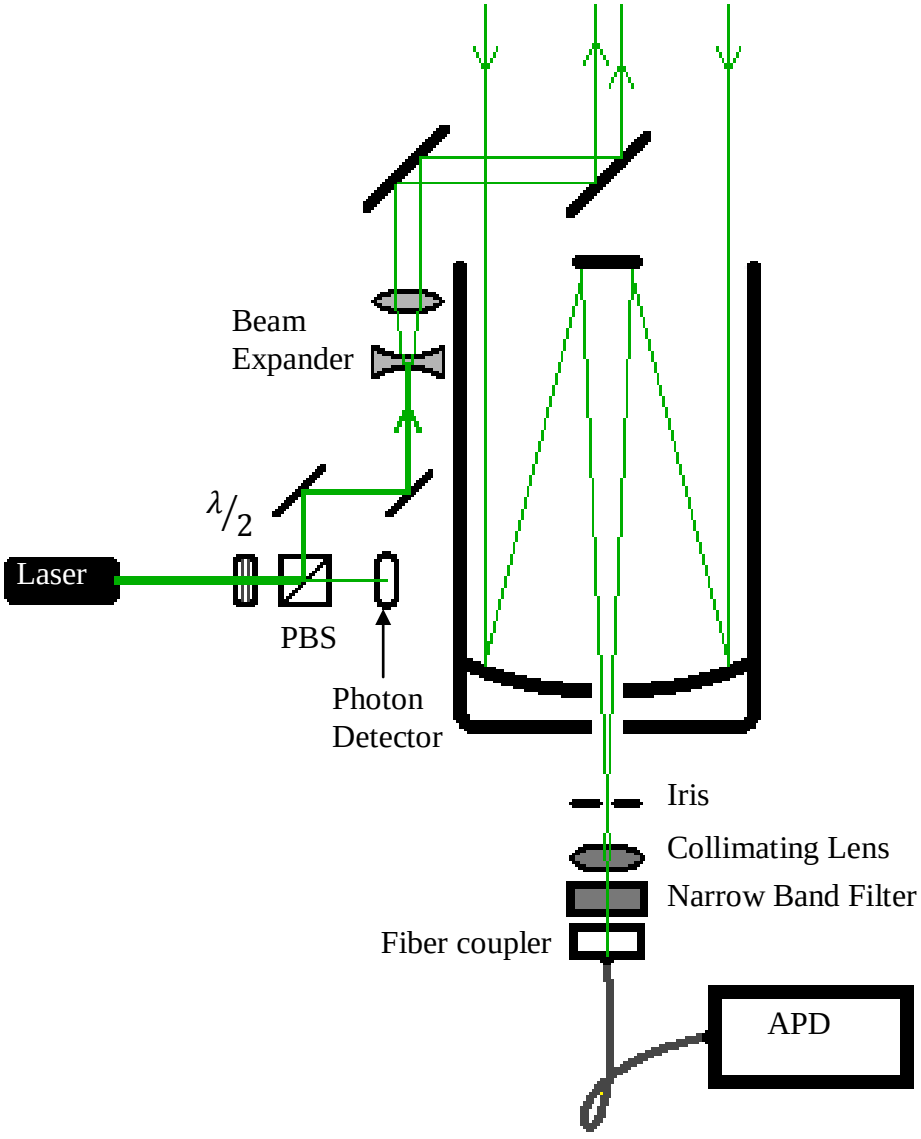


Figure (5) Schematic of the Micro-Pulse Lidar system.

Table (1) Transmission Parameters

| *Parameter* | *Measured Value* |
|---|---|
| Wavelength of Transmitted Beam | 532 nm |
| Energy per Pulse | >3 μJ |
| Pulse Width | <1 ns |
| Beam Waist at Output Plane | ≅1.95 cm |
| Pulse Repetition Frequency | ≅7.2 kHz |
| Beam Expansion | 10 X |
| Beam Expander RMS Wavefront Distortion | 0.0040λ |

Table (2) Receiver Parameters

| *Parameter* | *Measured Value* |
|---|---|
| Telescope Diameter | 278 mm |
| Telescope f/# | f/10 |
| Collimation Lens Focal Length | 250 mm |
| Narrow Band Filter Center Wavelength | 532 nm |
| Narrow Band Filter FWHM | 1 nm |
| Fiber Coupler N.A. | .5 |
| Fiber Coupler Focal Length | 11 mm |
| Fiber Coupler Clear Aperture | 1.8 mm |
| Fiber Optic Core Diameter | 105 μm |
| APD Efficiency at 532 nm | 54% |
| APD Dark Count Rate | ≅150 counts/s |
| APD Saturation Count Rate | 12 MHz |

The avalanche photodiode operating in the photon counting mode is monitored using a multi-channel scalar card (MCS) developed by Sigma Space. This MCS is capable of accepting four separate pulse inputs and simultaneously counting them based

on the input sync signal. The sync signal comes from the photodiode described previously. Once the sync pulse is received the MCS divides pulse inputs into time-of-flight bins for range differentiated data. The MCS then repeats this process for multiple returns to increase the signal to noise ratio up to a maximum of 5000 accumulations. Parameters such as number of bins, bin resolution, and number of accumulations to be integrated before data transfer, are set by a software control. The integrated data is then transmitted to the host CPU via the Universal Serial Bus 1.1 interface.

Labview has been chosen as the software control to define parameters for the MCS as well as collect, perform preliminary processing on, and save the returned signal. Upon initialization of the program, Labview defines the range-bins to be 7.5 m, and the total distance collected for each pulse to be 12 km. For minimal data transfers the maximum of 5000 accumulations is also defined. The data is then read in as a 1-D array. Corrections for high APD counts are performed based on the APD specifications of

$$c_a = \frac{c_o f - c_d}{\varepsilon}. \quad \{4\}$$

With $c_a$ being the actual photon count, $c_o$ the output photon counts, $c_d$ the dark count average of 150 counts/s, $\varepsilon$ the photon detection efficiency of 54%, and $f$ the correction factor found from

$$f = \frac{1}{1 - (t_d c_o)} \quad \{5\}$$

where $t_d$ is the dead time of 50 ns. The actual photon counts are then plotted along with range corrected returns, found by $r^2$ multiplication, for user monitoring. After an accumulation of 100 returns the program will add to the "waterfall" plot which is a false

color plot to view the history of data accumulation. At this point the returns are also saved. This creates a file with 500,000 laser pulse return signals averaged, thus a time average of 70 s. The user interface is shown in Figure (6). These saved return signals are then inverted as described in chapter three.

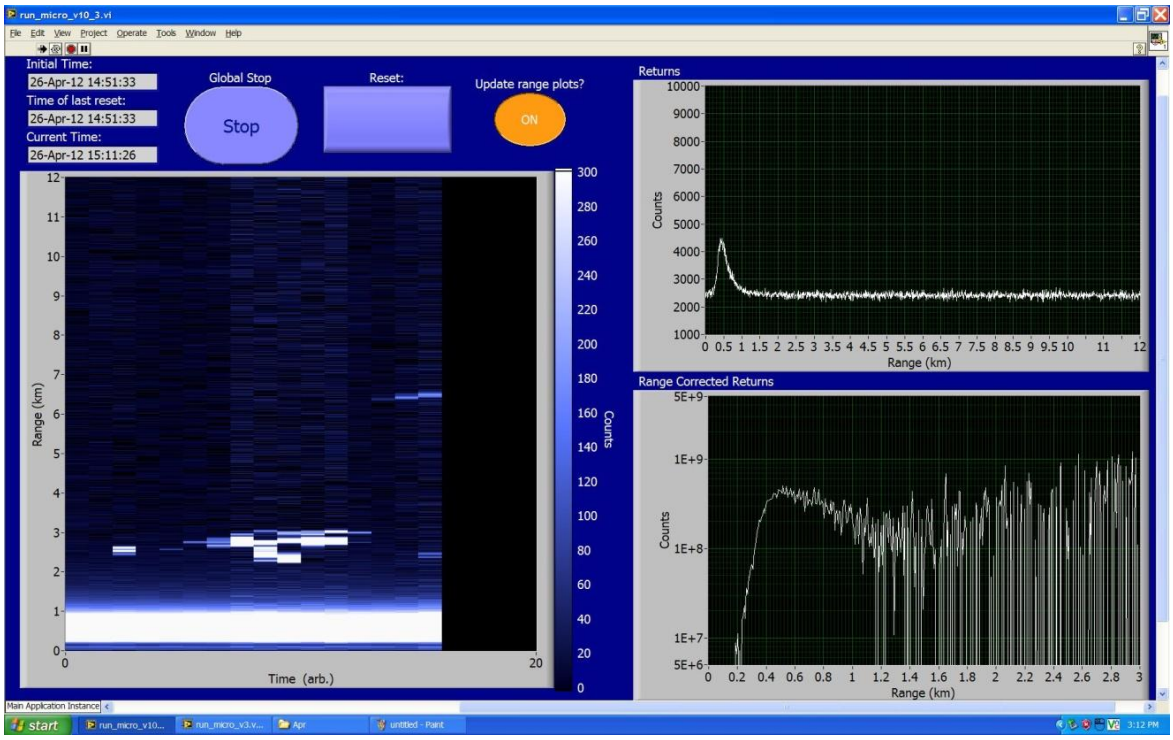


Figure (6) The Labview user interface displaying time, waterfall plot, returns and range corrected returns.

## Collimation

As mentioned above, the beam is re-collimated after exiting the barrel of the laser. The beam from the laser is approximately 2 mm in width and is subject to expansion based on

$$M^2 = \frac{\pi}{\lambda}\frac{d_B\theta}{2} \qquad \{6\}$$

where $M^2$ is the beam quality of the laser, $d_B$ is the diameter of the beam at the waist, and $\theta$ is the half-angle divergence of the beam. The beam quality is defined as the beam parameter product divided by $\frac{\lambda}{\pi}$, which is the beam parameter product of a diffraction limited Gaussian beam. This will of course result in a beam quality of 1 for a diffraction limited Gaussian beam and higher for anything else. The beam parameter product is defined as the divergence half angle times the beam waist radius. All these parameters are measurable and the manufacturer has determined the Nd:YAG laser used in the laser transmitter to have a beam quality of 1.3. With a constant beam quality, increasing $d_B$ will decrease the angle of diffraction. Considering the original beam and the expanded and re-collimated beam both with a beam quality of 1.3, the former will have a diameter of 1320 mm at 3 km and the later will have a diameter of 132 mm at the same distance. Thus without increasing the quality of the beam the effect of divergence has been reduced.

The beam expander shown in Figure (5) produces a collimated beam with a 20 mm diameter. This size was used for a few practical reasons. First, the beam is encased in a periscope prior to transmission thus a large diameter beam would result in a large diameter periscope. As this is protruding over the telescope to create a co-axial system; a large diameter periscope results in a large obstruction of the return signal. Second, creating a lidar that is eye-safe is desirable and requires low power. The power due to a beam diameter increase with constant energy, *E*, falls as

$$P = \frac{E}{\pi\left(\frac{d_B}{2}\right)^2}. \qquad \{7\}$$

Thus, a beam expanded to 20 mm will have 100 times less power than the 2 mm diameter beam. The maximum safe permissible exposure per pulse of 532 nm light is 0.0025 W/cm$^2$, the MPL with reduced power has 0.0022 W/cm$^2$ per pulse at the point of transmission. As this will decrease through the atmosphere due to expansion and scattering this is certainly safe for pilots of planes or helicopters to fly over. As apparent from the closeness of maximum power per pulse to the calculated power, maximum power was maintained while allowing for eye-safety. The lidar equation derived in chapter 3 will show the need for maximum transmitted power, as the amount of backscattered light is directly proportional to the power transmitted. The best return signal is created by maintaining as much power as possible and this has been achieved. Thus the beam has been expanded and re-collimated to create an eye-safe system that optimizes power.

## Field of View

In designing and setting up the MPL the field of view was considered for both the purpose of noise minimization and maximum overlap with the transmitted beam. As this system was primarily designed to study aerosols in the first 2 km of atmosphere, capturing as much of that range as possible was a driving goal. It is also useful to have signal from 9-12 km which corresponds to the high cirrus clouds. Thus the field of view, as determined by the telescope and receiver optics, must allow for a return signal from the entire range 0-12 km.

After a few calculations it will be seen that the field of view is entirely dependent on the diameter of the telescope, the numerical aperture of the fiber coupler and the diameter of the fiber, as calculated by Repasky (personal communication, May 31, 2012). First, consider the ray diagram for the focusing lens shown in Figure (7). From which the angles $\theta_1$ and $\theta_2$ can be approximated as

$$\theta_1 \cong \frac{D_f/2}{f_f}, \qquad \{8a\}$$

$$\theta_2 \cong \frac{D_f/2 - R}{f_f} \qquad \{8b\}$$

with $D_f/2$ the lens radius, $f_f$ the focal length and $R$ the maximum off axis distance that will enter the fiber placed at the focus. This leads to the angular difference of

$$\Delta\theta = \theta_1 - \theta_2 = \frac{R}{f_f}. \qquad \{9\}$$

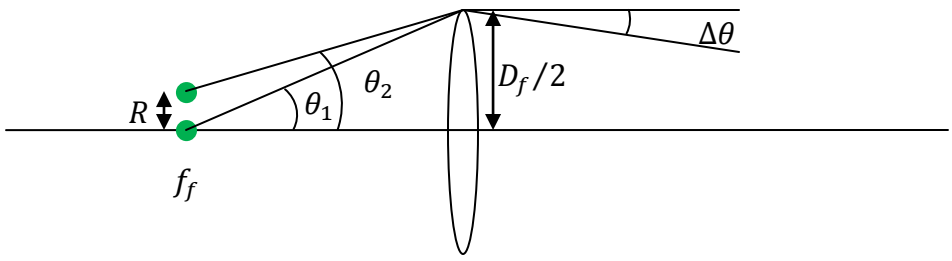


Figure (7) The ray diagram for the focusing lens is presented here. $f_f$ is the focus around which the fiber optic coupler will be positioned, the rest of the receiving optics lies to the right.

To determine $R$ consider the ray diagram including the collimating lens shown in Figure (8). Applying the thin lens equation twice the effective focal length of these two

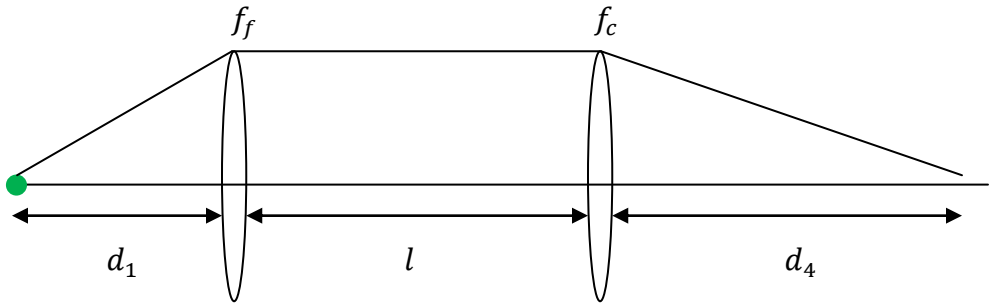


Figure (8) The ray diagram for the focusing lens and the collimating lens is presented here. The lens separation is $l$, the image distance $d_1$, the object created by the telescope is located at $d_4$, not depicted are the near infinite object and image locations $d_2$ and $d_3$.

lenses together is found. First the distance to an object that will form an image at $d_1$, will be $d_2$ found from

$$\frac{1}{d_2} = \frac{1}{f_f} - \frac{1}{d_1} = \frac{d_1 - f_f}{d_1 f_f} \qquad \{10\}$$

and thus

$$d_2 = \frac{d_1 f_f}{d_1 - f_f}. \qquad \{11\}$$

Note that for the image forming at the focus, $d_1 = f_f$, the distance to the object will approach infinity. This infinite focal distance implies a perfectly collimated beam. Continuing through the lens diagram the distance to the image plane for the collimating lens is simply

$$d_3 = l - d_2. \qquad \{12\}$$

Substituting equation $\{11\}$ for $d_2$ results in

$$d_3 = \frac{d_1 l - f_f l - d_1 f_f}{d_1 - f_f}. \qquad \{13\}$$

This image distance results from an object at $d_4$ found from the thin lens equation

$$\frac{1}{d_4} = \frac{1}{f_c} - \frac{1}{d_3}. \quad \{14\}$$

Substituting equation {13} into {14} leads to

$$\frac{1}{d_4} = \frac{1}{f_c} - \frac{d_1 - f_f}{d_1 l - f_f l - d_1 f_f}. \quad \{15\}$$

At this point let $d_1 = f_f$ which simplifies this quickly to

$$\frac{1}{d_4} = \frac{1}{f_c}. \quad \{16\}$$

Noting the that effective focal length of two lenses is defined as

$$\frac{1}{f_{eff}} = \frac{1}{f_1} + \frac{1}{f_2} \quad \{17\}$$

the effective focal length of the focusing and collimating lenses can then be found by using equation {16},

$$\frac{1}{f_{eff}} = \frac{1}{d_4} + \frac{1}{f_f}. \quad \{18\}$$

Solving equation {18} gives the effective focal length for $d_1 = f_f$

$$f_{eff} = \frac{f_f f_c}{f_f - f_c}. \quad \{19\}$$

The magnification of these two lenses for an object at the focal point of the collimating lens can now be found. Considering the lens diagram in Figure (9) the magnification is

$$M = \frac{R'}{R} = -\frac{f_c - f_{eff}}{f_{eff}}. \quad \{20\}$$

Using equation {19} this becomes

$$M = -\frac{f_c}{f_f}. \quad \{21\}$$

This magnification will result in a spot size of radius $R'$ at the focus of the telescope

$$R' = R\frac{f_c}{f_f}. \quad \{22\}$$

Substituting equation {22} into equation {9} will lead to the angular difference of

$$\Delta\theta = \frac{R'}{f_t} = \frac{Rf_c}{f_t f_f}. \quad \{23\}$$

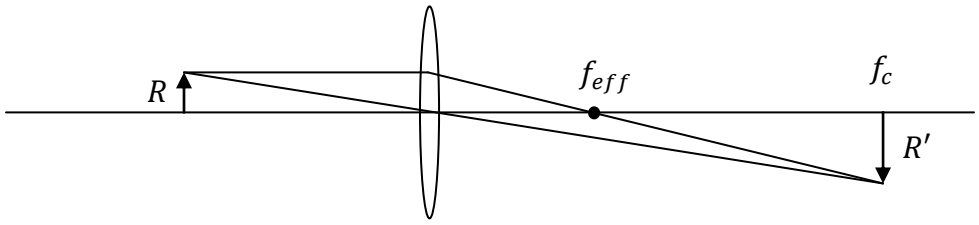


Figure (9) The ray diagram for the effective lens showing the total magnification of an object at $f_c$. The approximate position the telescope will focus light to.

The half angle field of view can be further simplified by the recognition that the $f/\#$'s for all the optics must match for the light hitting the fiber optic core to propagate down the fiber. Defining the $f/\#$ as

$$f/\# \equiv \frac{f}{D} \quad \{24\}$$

the numerical aperture of the fiber is defined for ease of notation as

$$N.A. = \frac{1}{2(f/\#)}. \quad \{25\}$$

Combining equations {24} and {25} leads to

$$D = 2f_f N.A. \quad \{26\}$$

This diameter $D$ can also be found geometrically from Figure (10) to be

$$2\theta \cong \frac{D_t}{f_t} \cong \frac{D}{f_c}. \quad \{27\}$$

Equation {27} can be substituted into {26}and solved for $f_c$ resulting in

$$f_c = \frac{2f_t f_f N.A.}{D_t}. \quad \{28\}$$

Equation {28} substituted into equation {23} leads to the half angle field of view of

$$\Delta\theta = \frac{R}{D_t} N.A. \quad \{29\}$$

From the quantities presented in Table (2) the MPL has half angle field of view of 190 μrad.

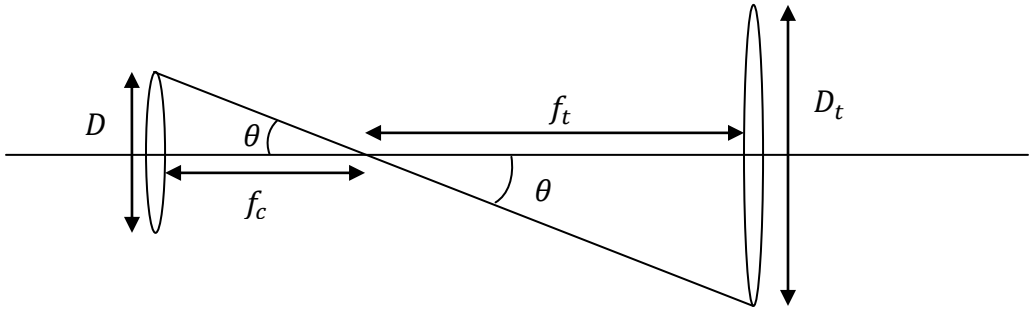


Figure (10) This is the ray diagram showing the relationship between $D$ and $D_t$.

From geometric optics, diffraction will slightly minimize this field of view as well. In a limit of no diffraction, a point imaging to a point will produce a field of view determined above. This point will have an extent of a circle of radius $r_c$ called the circle of least confusion found from

$$r_c = \frac{r_0 f}{R} \quad \{30\}$$

with $r_0$ the effective telescope radius, $f$ the effective focal length of the receiver optics before the fiber, and $R$ the distance to the point of radiation. Any off-axis radiation will form an image at $r_f$ away from the axis based on magnification as

$$r_f = \frac{rf}{R}. \qquad \{31\}$$

The result of these two effects is an image circle centered on $r_f$ of radius $r_c$ as shown in Figure (11). Diffraction will thus decrease the amount of light gathered from off-axis points and the noise from off-axis radiation will be minimized. This effect will have minimal impact on the signal provided the co-axial system is aligned.

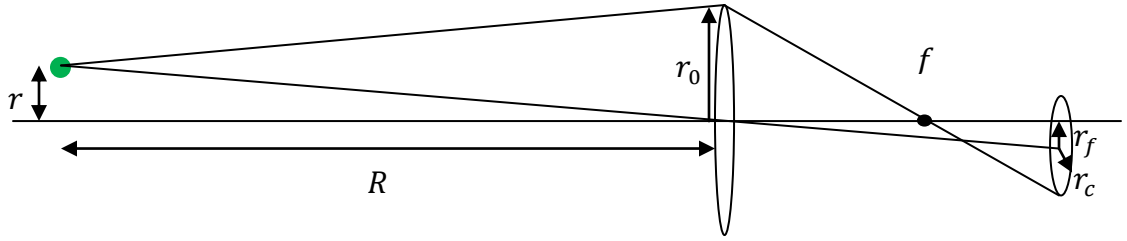


Figure (11) The ray diagram incorporating diffraction.

In discussing the field of view to this point the center obscuration in the Schmidt-Cassegrain telescope has been ignored. As can be seen in Figure (12) and Figure (13 a) the center obscuration allows various portions of a Gaussian beam's return signal to be retrieved. Should the beam be transmitted from the side of the telescope, the returns will be very non-symmetric below full overlap as depicted in Figure (13 b). As shown in Figure (12) a transmission over the center of the obscuration will have a symmetric return or cross-section of the beam and allow for easy employment of an overlap function. A detailed discussion of the overlap function is presented in Chapter 3.

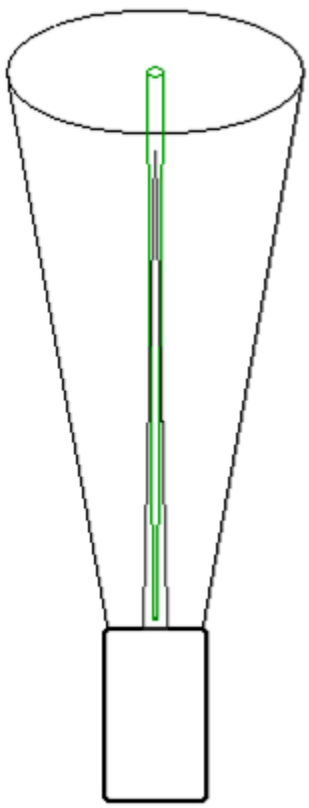

Figure (12) The transmitted beam is expanding throughout the range shown to eventually overcome the obscuration and careful alignment maintains the beam in the field of view of the telescope for the next 12 km.

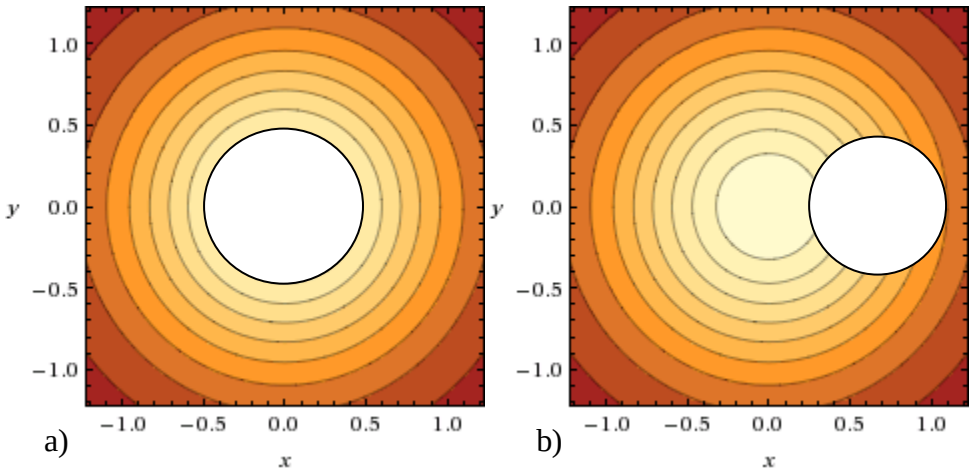


Figure (13) a) Gaussian beam cut symmetrically by the obscuration and b) Gaussian beam cut non-symmetrically by obscuration moving horizontally through the diameter of the beam.

## Noise

Aside from geometrically induced errors, the signal returned is subject to detection errors. The noise the APD receives can often become larger than the signal making retrievals impossible. For this system the signal to noise ratio has been calculated using the theory as derived by Kovalev [13]

$$\frac{S}{N} = \frac{N'_{ph}\sqrt{pt}}{\sqrt{N'_{ph} + 2(N'_b + N'_d)}} \quad \{32\}$$

where $N'_{ph}$ is photon counts of the signal per second, $N'_b$ is background counts per second, and $N'_d$ is dark counts per second. This is calculated for a certain time, $t$, and summed signal pulses $p$, and as can be seen the shorter the measurement the worse the ratio gets. Dark counts for the APD used in the lidar receiver are less than 150 counts/s. Background counts vary between 0 and $17\times10^2$ counts/s depending greatly on the sun and cloud cover. It is notable that cloud cover can either increase or decrease background counts depending on the angles between the sun, the cloud, and the MPL. Signal counts can be found by subtracting the background counts and the dark counts from the total signal to give a typical return signal as a function of range shown in Figure (14). This will result in the signal to noise ratio seen in Figure (15) for this APD operating in the MPL system. These values have been improved by averaging multiple returns together.

As can be seen in Figure (15) the signal to noise ratio falls as a function of range. The signal to noise ratio never falls below 1 for the range of retrieval. A ratio of 1 is the threshold for extracting information out of the return. All retrievals for the MPL have 500,000 pulses averaged, which assists in gaining these high signal to noise ratios.

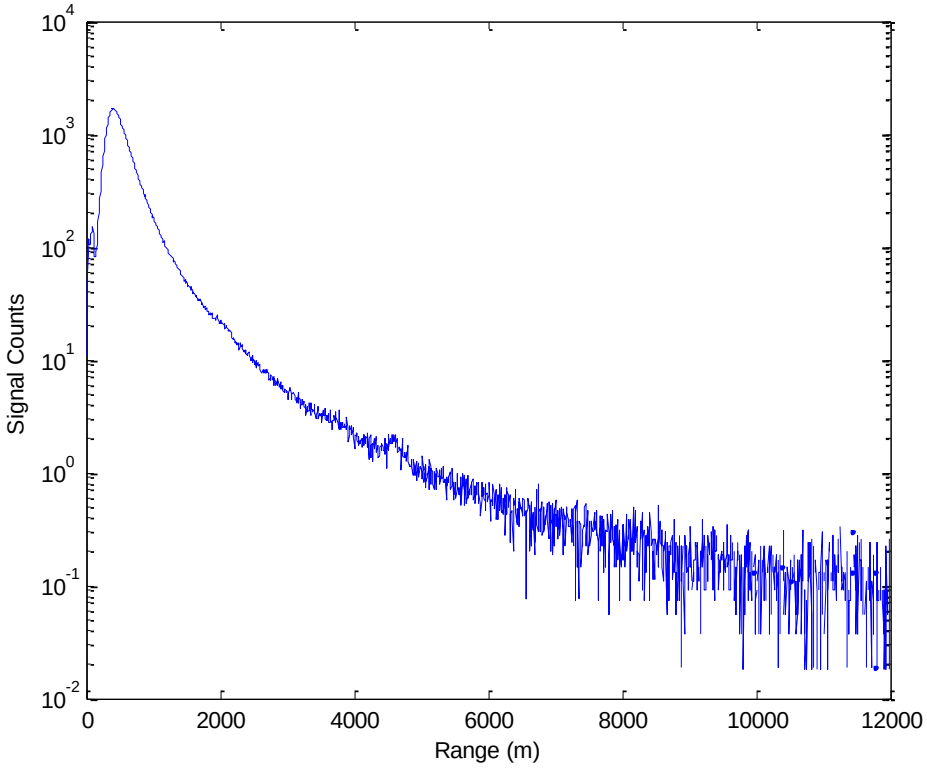


Figure (14) Signal Counts as a function of range found for the MPL

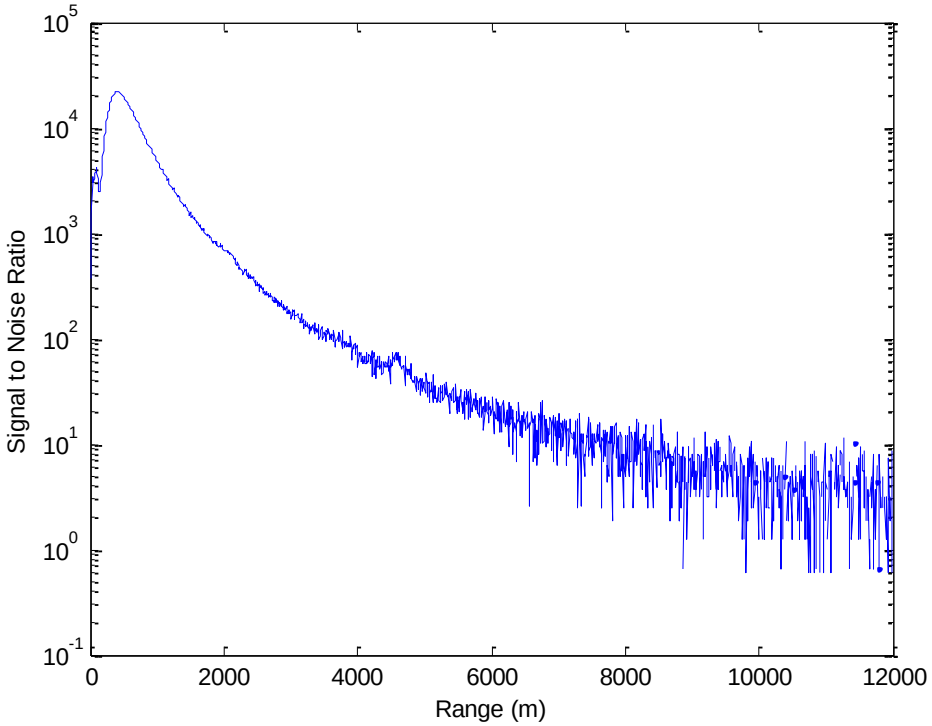


Figure (15) Signal to Noise Ratio as a function of range found for the MPL. As the ratio nears 1 the information in the return is lost in the noise.

# CHAPTER THREE – LIDAR RETREAVAL

## Derivation of the Lidar Equation

The lidar equation is used to describe the signal collected by the lidar as a function of the instrument and atmospheric parameters. The derivation follows the work of Fricke-Begemann [14]. When a plane wave hits a scatterer in general the intensity scattered into the solid angle $d\Omega$ will be dependent on the direction $\theta$ so that

$$\left(\frac{dI}{d\Omega}\right)_\theta = \frac{I_0}{A}\left(\frac{d\sigma}{d\Omega}\right)_\theta N \quad \{33\}$$

with $A$ and $N$ being the area and number of scatterers in the volume considered, respectively, and $I_0$ the incident beam intensity. Here $\sigma$ is the total optical cross-section of the scattering volume, thus, $\frac{d\sigma}{d\Omega}$ is the differential scattering cross-section.

As $\theta$ will always be $\pi$ in the case of lidar received intensity, the backscatter coefficient, $\beta$, is defined for ease of notation as

$$\beta = \rho\left(\frac{d\sigma}{d\Omega}\right)_\pi \quad \{34\}$$

where $\rho$ is defined to be the density of scatterers in the volume $V = Adr$. Thus the intensity scattered into the solid angle can be re-written as

$$\left(\frac{dI}{d\Omega}\right)_\pi = I_0 dr\beta. \quad \{35\}$$

With the solid angle defined as

$$\Omega = \iint_S \frac{\hat{n}\cdot d\vec{A}}{r^2} \quad \{36\}$$

moving $d\Omega$ to the right-hand side in equation {35} and integrating will result in the lidar equation

$$(I)_\pi = I_0 dr\beta \frac{A}{r^2}. \quad \{37\}$$

Here the integrated solid angle $\frac{A}{r^2}$, is the effective receiving area of the telescope. Note that this equation is valid for an ideal lidar system operating without beam attenuation. Considering a non-ideal system, the efficiency factor, $\eta < 1$, is added due to losses in the fiber optic cable and photon detector. Similarly, accounting for the geometric optical constraints, which limit returns close to the system, an overlap factor dependent on range, $O(r)$, is added; this is further discussed in Chapter 2. The non-ideal lidar equation can now be written as

$$(I)_\pi = I_0 dr\beta \frac{A}{r^2} \eta O(r) \quad \{38\}$$

Next, consider that the intensity reaching the scatterer at $r$ is not that which left the transmitter, but has been attenuated through the atmosphere by the atmospheric transmission, T. The atmospheric transmission is related to the optical depth, $\tau$, so that

$$TI_0 = e^{-\tau} I_0. \quad \{39\}$$

As each section of air is traversed twice by light before detection in a lidar receiver, this transmission will be squared, as discussed by Fernald et al. [15]. Finally the elastic lidar equation is

$$(I)_\pi = I_0 dr\beta(r) \frac{A}{r^2} \eta(\lambda) O(r) T^2. \quad \{40\}$$

By defining two new variables the lidar equation can be greatly simplified, this process is seen in both Nehrir's [16] and Hoffman's [17] work. First, all the instrument

specific quantities: $I_0$, $dr$, $A$, and $\eta(\lambda)$ can be absorbed into a calibration constant $C_0$. As the returns are collected by received power it will be useful to substitute $I(r) = \frac{P(r)}{A}$ and also absorb $A$ into $C_0$. Second, the optical power and squared range can be combined to create a range corrected return $L(r) = P(r)r^2$. These two variables substituted into {40} result in a lidar equation of the form

$$L(r) = C_0\beta(r)T^2(r)O(r). \quad \{41\}$$

Two Component Atmosphere

The atmosphere is typically modeled using Mie scattering from atmospheric aerosols and Rayleigh type scattering for atmospheric molecules. This model is referred to as a two component atmosphere. The lidar equation has two variables which are specifically dependent on these two components. These variables are the backscatter and extinction coefficients; where the extinction, $\sigma(r)$, is defined in relation to the transmission as

$$T^2 = \exp\left(-2\int_0^r \sigma(r')dr'\right). \quad \{42\}$$

The backscatter coefficient can be split into its molecular and aerosol components, and written as

$$\beta_{total}(r) = \beta_m(r) + \beta_a(r) \quad \{43\}$$

where $\beta_m(r)$ is the molecular backscatter and $\beta_a(r)$ is the aerosol backscatter. Similarly the extinction can be written as

$$\sigma_{total}(r) = \sigma_m(r) + \sigma_a(r) \quad \{44\}$$

where $\sigma_m(r)$ is the molecular extinction and $\sigma_a(r)$ is the aerosol extinction. This leads to a separable transmission of

$$T^2(r) = T_m^2(r)T_a^2(r) = exp\left(-2\int_0^r [\sigma_m(r') + \sigma_a(r')]\, dr'\right). \quad \{45\}$$

Using the two component model, the molecular lidar ratio is defined as $S_m = \frac{\sigma_m(r)}{\beta_m(r)}$ and the aerosol lidar ratio is defined as $S_a = \frac{\sigma_a(r)}{\beta_a(r)}$. Both of these ratios are assumed to be constant with respect to altitude to allow for the inversion of the lidar data based on the Fernald lidar retrieval method [15]. The molecular lidar ratio resulting from scattering from small spheres is $\frac{8\pi}{3}$ sr [13].

The Rayleigh backscatter has been found to be entirely dependent on the pressure as a function of height, $P(h)$, the temperature as a function of height, $T(h)$, and wavelength, thus it can be modeled using [13]

$$\beta_m(r) = \frac{374.28\,\frac{P(h)}{T(h)}}{\lambda^4}. \quad \{46\}$$

This, along with the molecular lidar ratio, results in a modeled molecular extinction of

$$\sigma_m(r) = \frac{8\pi}{3}\frac{374.28\,\frac{P(h)}{T(h)}}{\lambda^4}. \quad \{47\}$$

## Lapse Rate

To complete the modeled molecular returns the temperature as a function of height is needed. For a static adiabatic atmosphere, this temperature profile can be estimated using

$$T(h) = T_0 - \Gamma h \quad \{48\}$$

with Γ being the lapse rate and $T_0$ the ground temperature. The lapse rate for a dry adiabatic atmosphere is easy to reduce from statistical mechanics considerations as seen in Wallace's work [5]. With the definition of the specific heat at constant pressure, $c_p = \left(\frac{\partial Q}{\partial T}\right)_p$, and considering only a dry parcel of air, the change in temperature with respect to height, the adiabatic lapse rate, is

$$-\frac{dT(h)}{dh} = \frac{\boldsymbol{g}}{c_p} \equiv \Gamma_{\mathrm{d}} \quad \{49\}$$

using $\boldsymbol{g}$= 9.81 m/s$^2$ and $c_p = 1001$ J K$^{-1}$ results in $\Gamma_{\mathrm{d}} = 9.8$ K km$^{-1}$. The actual lapse rate is typically less and is dependent on many atmospheric properties including relative humidity. The pressure can be modeled with the same lapse rate as [13]

$$P(h) = P_0 \left[\frac{T_0}{T(h)}\right]^{-\frac{0.034164}{\Gamma}} \quad \{50\}$$

These models can be compared with the measured temperature and pressure profiles as found by satellite. The satellite Aqua flies over Bozeman every few days as part of the A-train. It creates temperature and pressure profiles from its position to the ground using the Atmospheric Infrared Sounder and the Advanced Microwave Sounding Unit. Examples of the temperature and pressure profiles are shown in Figure (16) and Figure (17) respectively. As can be seen, in the range below 11 km the temperature profile is a linear decay with a slope of 7.5 K km$^{-1}$ which is the lapse rate for this day.

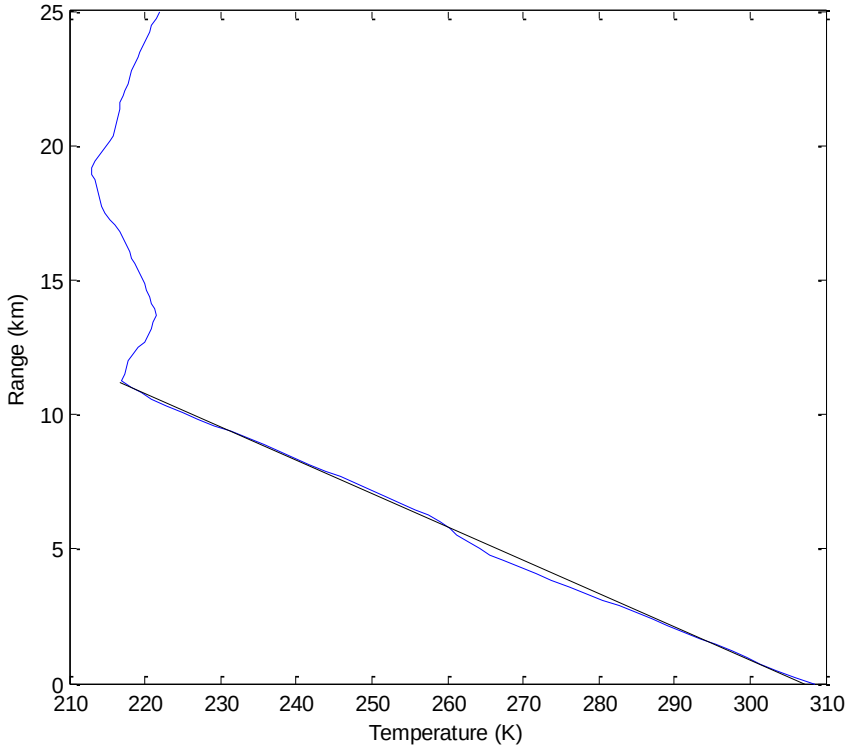


Figure (16) Aqua temperature profile in blue, linear lapse rate in black.

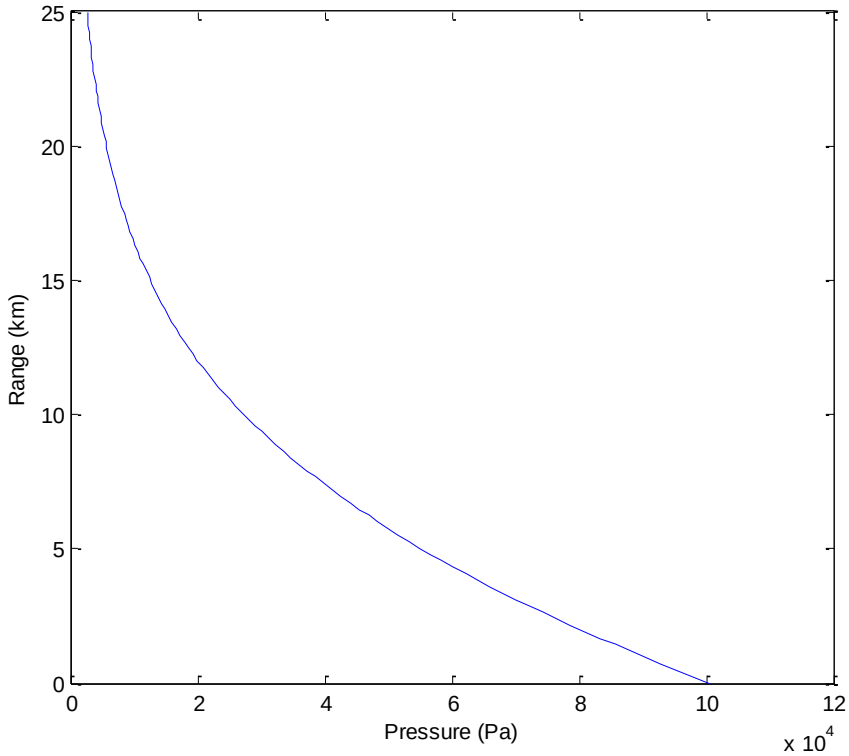


Figure (17) Aqua pressure profile.

## Atmospheric Boundary Layer

The ABL height, $r_0$, is an important atmospheric thermodynamic property and plays important roles in weather, transport, and atmospheric chemistry. The ability to monitor this height has many observational uses as the dynamics at the top of the ABL have been shown to govern the transport and concentrations of pollutants at the bottom of the ABL. This height has been defined in many different ways for varying purposes. Kovalev [13] outlines 17 different definitions for this layer. For this work the definition used will be the point at which the aerosol backscatter term drops to 0 $sr^{-1}m^{-1}$, or the first discontinuity in the aerosol concentration profile. This value is useful to monitor on its own, though it is also used at many points in the inversion to distinguish between the modeled terms above the ABL and the aerosol dependent terms below.

## Calibration Constant

The calibration constant, though a purely instrument dependent quantity, is easiest to find experimentally through a partial inversion. The lidar equation {41} can be solved for the calibration constant above the boundary layer,

$$C_0(r) = \frac{L(r)}{\beta(r)T_a^2(r)T_m^2(r)O(r)}. \qquad \{51\}$$

As this is above the ABL $T_a^2(r)$ is the total transmission through the atmospheric aerosols and is found using aerosol optical depths, measured with a solar radiometer which is a part of the NASA Automated Robotic Network (AERONET) [18]. $T_m^2(r)$ is the transmission due to molecular components of the atmosphere, found using the modeled

extinction. Being above the boundary layer both allows the overlap function to be 1 and the backscatter to be entirely the modeled molecular return.

## Inversion

The lidar data includes the return signal as a function of range as described by the lidar equation. The fundamental aerosol properties including the backscatter, extinction and lidar ratio are retrieved by inverting the lidar data. This work will follow the inversion technique developed by Fernald et al. [15]. With the Rayleigh model, the lapse rate, and the experimentally found calibration constant and overlap function, the unknowns are the aerosol backscatter, extinction, and lidar ratio. By solving a differential equation the lidar equation can be reformulated to find the aerosol backscatter and with the use of AERONET transmission data the lidar ratio can be found.

After including the two component atmosphere by substituting {43} and {44} into {41}, the lidar equation can be written as

$$L(r) = C_0\big(\beta_m(r) + \beta_a(r)\big)T_m^2(r)T_a^2(r)O(r). \quad \{52\}$$

For purposes seen shortly this can be rewritten as

$$T_a^2(r) + \frac{\beta_m(r)}{\beta_a(r)}T_a^2(r) = \frac{L(r)}{C_0 T_m^2(r)\beta_a(r)}. \quad \{53\}$$

Multiply by $-2\sigma_a(r)$ and substituting the aerosol lidar ratio results in

$$-2\sigma_a(r)T_a^2(r) - 2S_a\beta_m(r)T_a^2(r) = \frac{-2S_a L(r)}{C_0 T_m^2(r)}. \quad \{54\}$$

Now considering

$$\frac{d\,T_a^2(r)}{dr} = -2\sigma_a(r)T_a^2(r), \quad \{55\}$$

substitution of {55} for the first term in equation {54} will yield the differential equation

$$\frac{d\,T_a^2(r)}{dr} - 2S_a\beta_m(r)T_a^2(r) = \frac{-2S_aL(r)}{C_0T_m^2(r)}. \quad \{56\}$$

Solving this for $T_a^2(r)$ results in an aerosol transmission independent of the aerosol extinction

$$T_a^2(r) = e^{2S_a\int_0^r \beta_m(r')dr'}\left\{1 - \frac{2S_a}{C_0}\int \frac{L(r')}{T_m^2}e^{2S_a\int_0^{r'}\beta_m(r'')dr''}dr'\right\}. \quad \{57\}$$

The lidar equation {52} can now be written in terms of the total backscatter $\beta_t(r)$, the aerosol lidar ratio $S_a$, and molecular and geometrical quantities $C_0$, $O(r)$, $T_m^2(r)$, and $\beta_m(r)$

$$L(r) = C_0\beta_t(r)T_m^2(r)e^{2S_a\int_0^r \beta_m(r')dr'}\left\{1 - \frac{2S_a}{C_0}\int \frac{L(r')}{T_m^2(r')}e^{2S_a\int_0^{r'}\beta_m(r'')dr''}dr'\right\}O(r). \quad \{58\}$$

Solving for the total backscatter the only unknown is the aerosol lidar ratio

$$\beta_t(r) = \frac{L(r)e^{-2S_a\int_0^r \beta_m(r')dr'}}{C_0O(r)T_m^2(r) - 2S_aO(r)\int \frac{L(r')}{T_m^2(r')}e^{2S_a\int_0^{r'}\beta_m(r'')dr''}dr'}. \quad \{59\}$$

Substituting this into {43} results in the aerosol backscatter of

$$\beta_a(r) = \frac{L(r)e^{-2S_a\int_0^r \beta_m(r')dr'}}{C_0O(r)T_m^2(r) - 2S_aO(r)\int \frac{L(r')}{T_m^2(r')}e^{2S_a\int_0^{r'}\beta_m(r'')dr''}dr'} - \beta_m(r). \quad \{60\}$$

At this point by positing an aerosol lidar ratio $S_a$ the aerosol extinction $\sigma_a(r)$ can be solved for. The aerosol optical depth (AOD) defined as $\int_0^{r_0}\sigma_a(r')dr'$ can be matched with known AOD data from AERONET transmissions. As the AOD is directly proportional to the $S_a$ the error in this match can be used to change the posited $S_a$ and improve the match.

Inverting the data this way results in aerosol backscatter and extinction coefficients as well as time resolved lidar ratios, lapse rates, and boundary layer depths.

## Calculation of Input Parameters

### Overlap Function

Performing the inversion requires the following parameters to first be calculated. Starting with the first correction performed on returns, the overlap function. This function is often called the geometrical form factor because of its pure dependence on the geometry of the receiver optics. The obscuration in the telescope, the field of view of the telescope, and the desire to stay in overlap at long distances are major factors in determining the probability that backscattered light from close ranges will hit the detector as is discussed in detail in Chapter 2.

This overlap function is found experimentally by operating the lidar in a horizontal configuration that takes advantage of a constant, well mixed atmosphere as discussed in Nehrir's work [16]. This lidar was built so as to be easily rotated for this purpose, it was mounted on a 3 dimensionally rotating tripod. By plotting the range corrected return signal, on a log-scale plot the linear nature of the return signal is evident after complete overlap is achieved beyond 1 km as shown in Figure (18).

The overlap function can be calculated using the measurement shown in Figure (18). From the lidar equation taking the natural log results in

$$\ln[L(r)] = \ln[O(r)] + \ln[C_0\beta(r)] - 2\sigma r \qquad \{61\}$$

where $\beta$ and $\sigma$ are assumed to be constant due to the well mixed atmosphere and horizontal operation. Beyond 1 km where overlap is achieved, the above equation reduces to

$$\ln[L(r)] = \ln[C_0\beta(r)] - 2\sigma r. \quad \{62\}$$

Fitting a straight line to the measured returns beyond 1 km yields

$$\ln[L(r)] = \ln[O(r)] - 0.000155r + 19.277. \quad \{63\}$$

The overlap function can now be determined by correcting the measured $\ln[L(r)]$ signal so that it falls on the linear fit below 1 km. This overlap function as a function of range is shown in Figure (19).

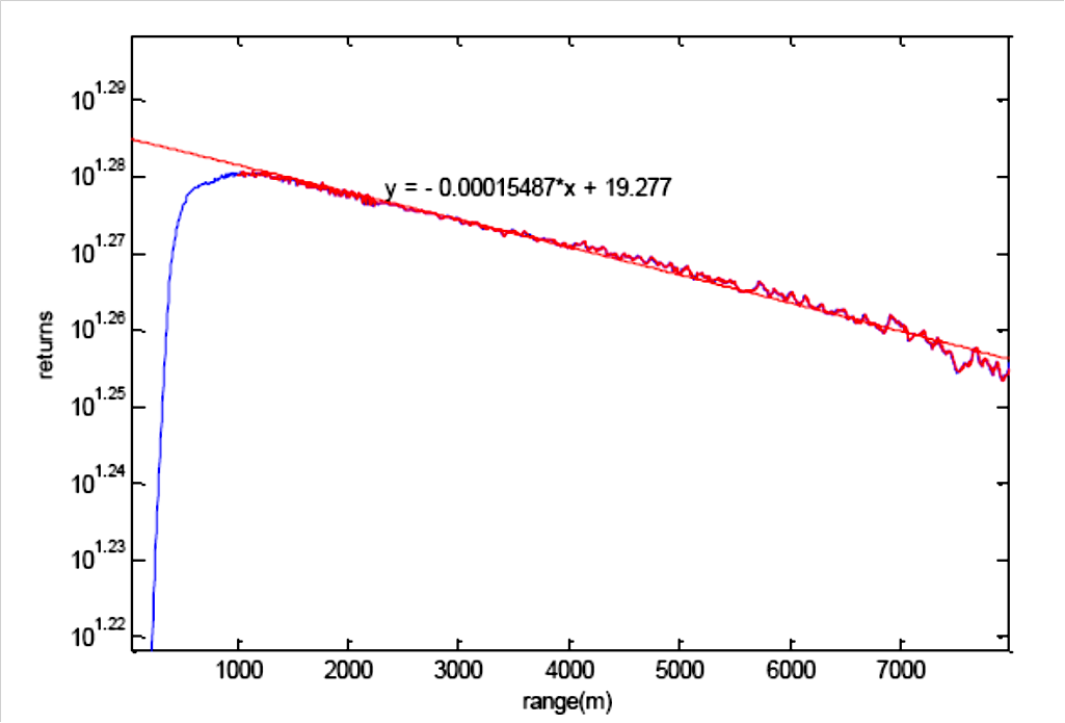


Figure (18) The horizontal lidar return in plotted on a log scale plot and the linear fit after full overlap has been found.

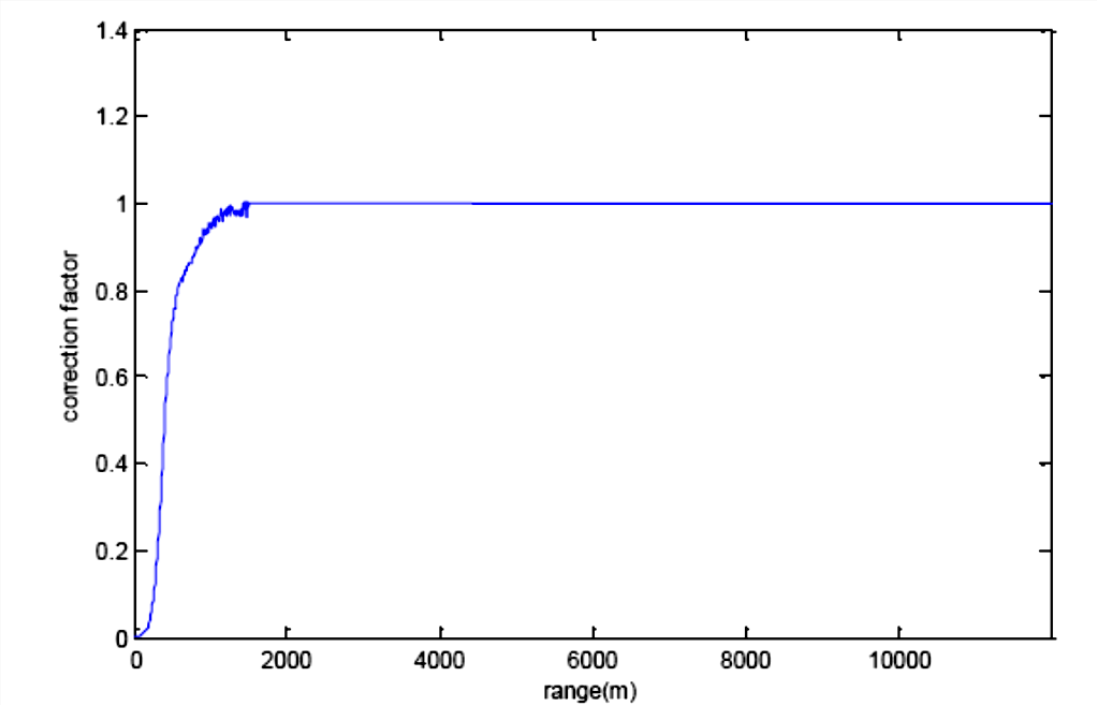


Figure (19) The overlap function for the entire range of the system has been found. After full overlap has been reached the function has been taken to be 1.

Lapse Rate

The second parameter, which is used in the modeled molecular backscatter as seen in equation {46}, is the lapse rate. The adiabatic lapse rate of 9.8 K $km^{-1}$ is the maximum tropospheric lapse rate, with the accepted average being 6.5 K $km^{-1}$. However, a more accurate lapse rate can be found, producing more accurate molecular models, by matching the slopes of the produced model with the slope of the inverted total backscatter. Should the slopes not match in the region where the returns are dominated by Rayleigh scattering the lapse rate is changed. Matching the slopes computationally is done using a Gaussian noise approximation of total backscatter around the modeled backscatter. The results of this process are presented in Figure (20).

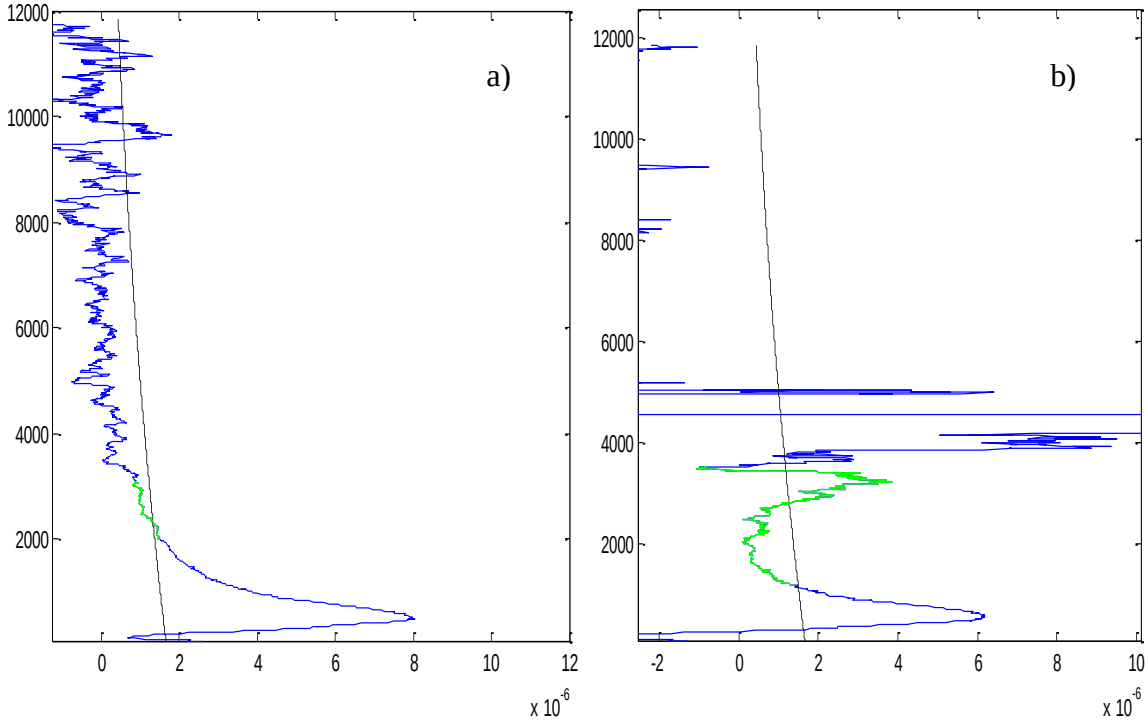


Figure (20) These figures show the total backscatter as inverted from the return in blue and the modeled Rayleigh backscatter in black. The green is the region for which Gaussian noise is expected above the boundary layer. As can be seen the slope mismatch has been corrected by allowing the lapse rate to vary between the start a) and the end b).

Calibration Constant

The third parameter needed for inversion is the calibration constant. Using equation {51} and the molecular model found above a range dependent constant is found. By looking at the region of atmosphere above the boundary layer, where the return is dominated by Rayleigh scattering, an average can be taken to find the constant. Figure (21) shows a plot of this calibration constant as a function of range. By averaging over the range 4 km to 6 km the calibration constant is determined to be $4.34\times10^{14}$ $Wm^3sr$.

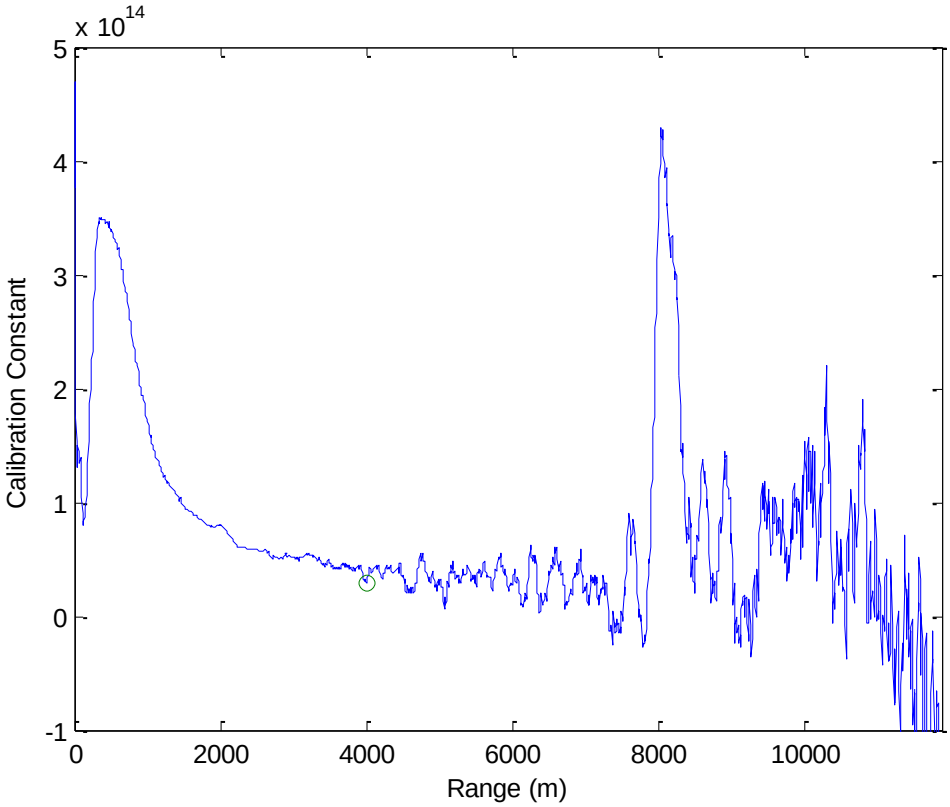


Figure (21) This figure shows the range dependent calibration constant. Above the boundary layer and before the range correction amplifies the noise, 4 to 6 km, this is a roughly constant value and by taking the average of values in that region a single calibration constant for this return is obtained.

# CHAPTER FOUR – DATA FROM THE MIRCO-PULSED LIDAR

## Results

The results presented in this chapter will include the backscatter and extinction coefficient profiles found by the above inversion technique performed on the MPL returns. The aerosol optical depths as correlated to the known transmission data are presented as a function of time. Also included are the resulting time-differentiated lidar ratios, lapse rates, and ABL heights. The time-differentiated calibration constants are included as a verification of their consistency over time. First, the returns from the 26$^{th}$ of June were taken as the Calipso satellite passed over Bozeman, allowing for comparison of the Caliop instrument and the MPL.

### June 26$^{th}$ 2012

The Calipso satellite maintains orbit with the A-train which includes the previously mentioned Aqua satellite and passes over Bozeman, Montana every few weeks. Shown in Figure (22) is the Caliop lidar data retrieved before and after the overpass plotted against location and range. The lidar data retrieved from the return at 45.6$^{\circ}$ N, 111$^{\circ}$ W was found to have a lidar ratio of 40 sr. The MPL returns are shown in Figure (23) with the results of the presented inversion shown in Figure (24). The lidar ratio retrieved from the MPL data was an average of 38 sr, validated by Caliop data. With the high AOD of .16, gained from AERONET data and shown in Figure (24 a), and multiple fires in Eastern and Northern Montana on this day, these lidar ratios, indicating a smoke filled atmosphere, were expected.

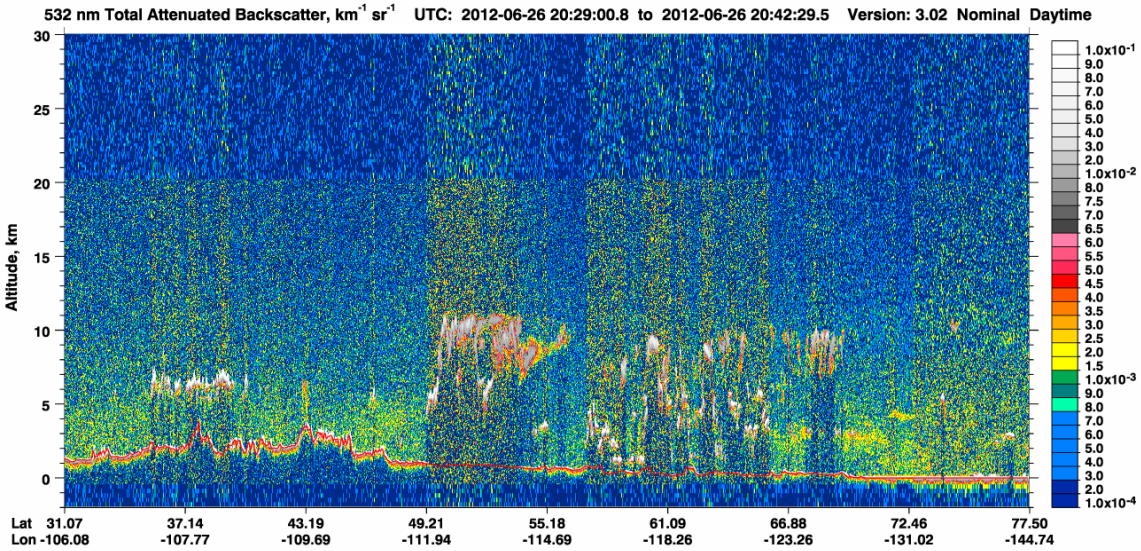


Figure (22) The Caliop lidar data, the red line plots the approximate ground level [18].

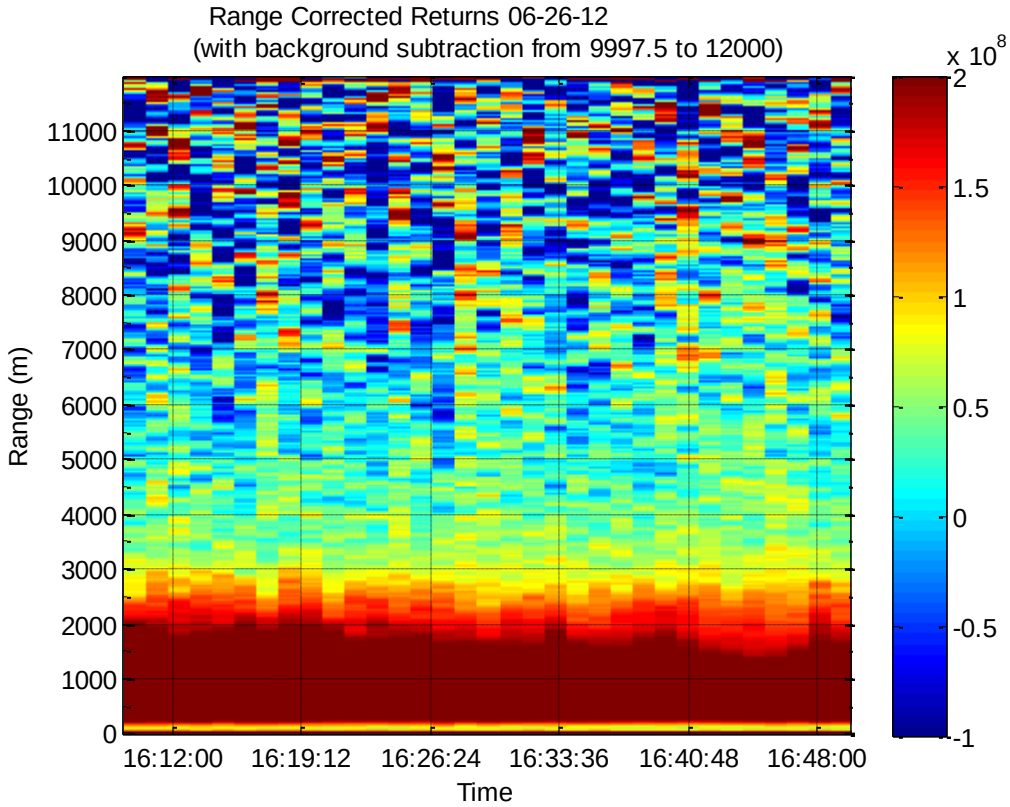


Figure (23) The MPL range corrected returns corresponding to the Calipso overpass.

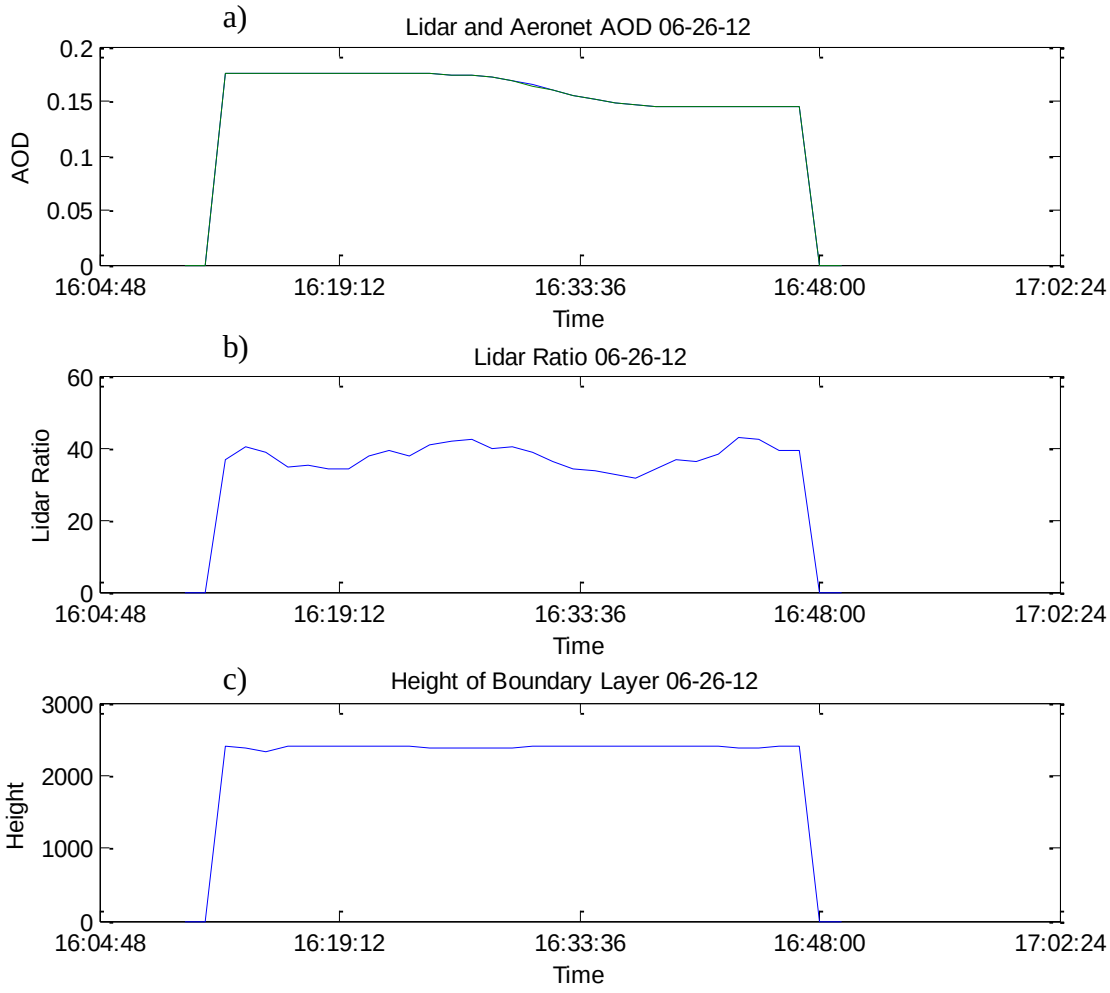


Figure (24) a) The MPL AOD is plotted in blue and the AERONET AOD plotted in green. b) The MPL lidar ratio. c) The height of the boundary layer.

In addition the lapse rate and calibration constant are presented in Figure (25). The lapse rate was found to be approximately the accepted average of 6.5 K/km. The calibration constant is also seen to be approximately constant throughout the inversion. The retrieved backscatter and extinction coefficients are shown in Figure (26) for later comparison.

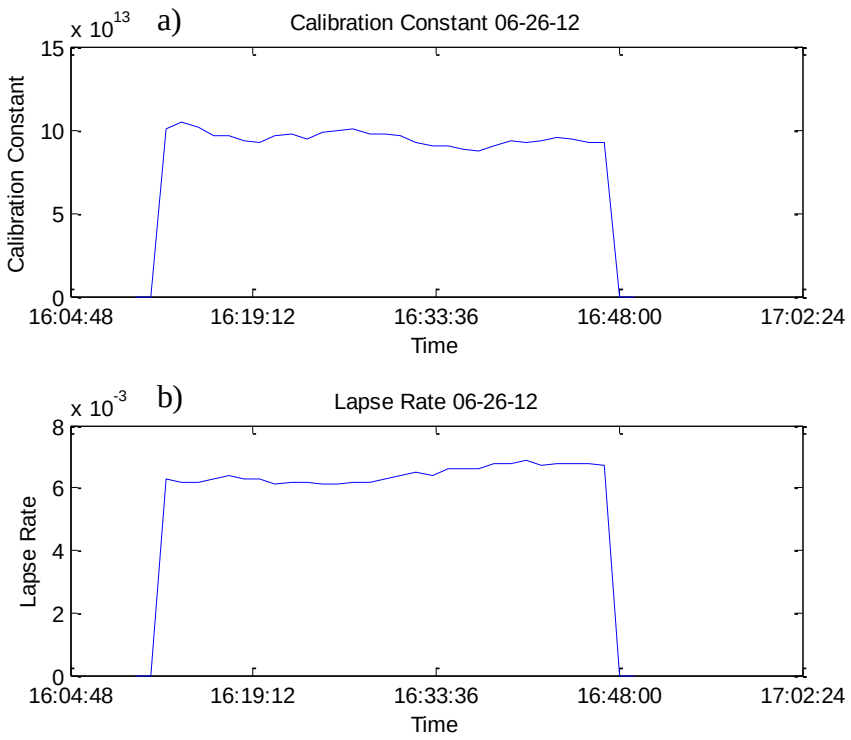


Figure (25) a) The calibration constant. b) The lapse rate of the accepted average

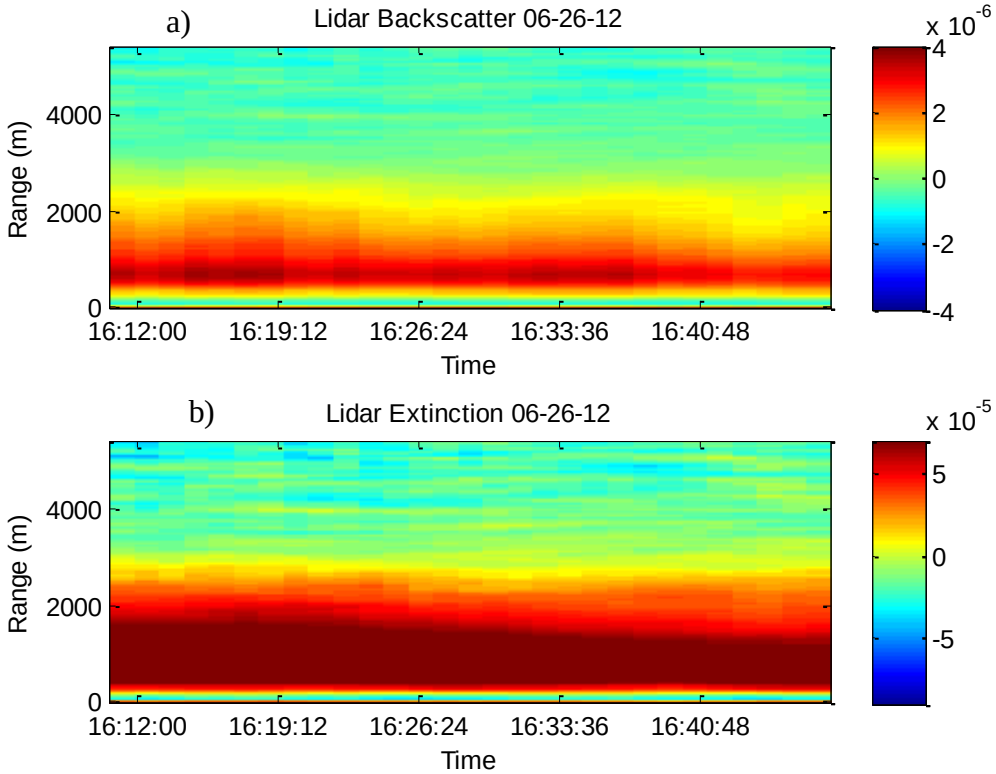


Figure (26) a) The backscatter coefficient intensity. b) The extinction coefficient intensity.

June 5th 2012

Data was again collected for the atmospheric conditions on the 5th of June. AERONET data was again used and the inversion was performed following the methods presented. The range corrected returns are shown in Figure (27). A single return is plotted in Figure (28). Note the large spike on top of the existing peak. This in itself is indicative of smoke in the troposphere. The smoke above Bozeman on this day was due to a fire near Norris, Montana. The aerosols here form a continual layer in the ABL.

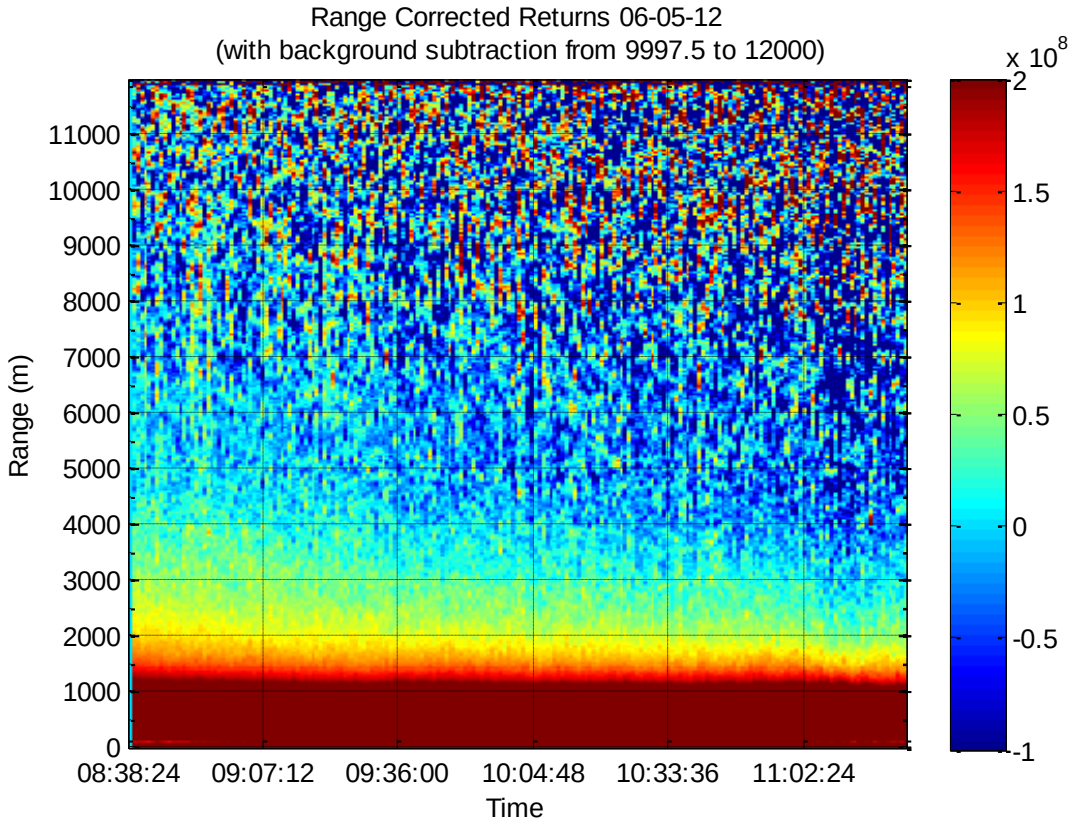


Figure (27) The range corrected returns for June 5th.

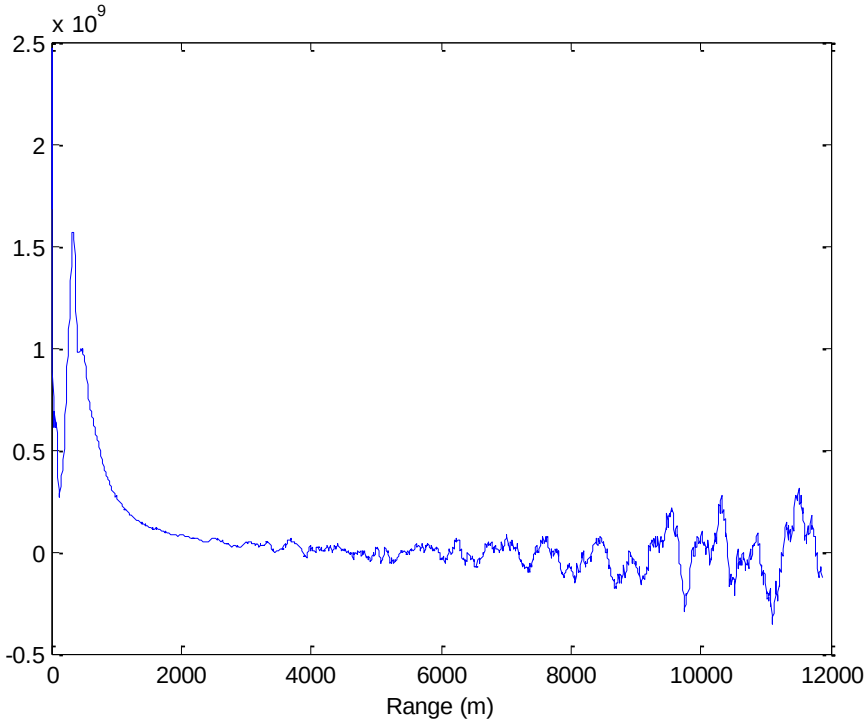


Figure (28) A single profile for the returns on June 5th. The typical gradual peak has the addition of the strong peak from smoke at 500 m.

The aerosol backscatter and extinction coefficient intensity profiles shown in Figure (29) are contrasted with the profiles seen in Figure (26). These plots indicate a difference of lidar ratio seen in Figure (30). The average lidar ratio here is much lower averaging 10 sr compared to the 40 sr on the 26th. This indicates a smaller average particulate size or a lower absorption. As this is the same particulate species this difference can be attributed to the nearness of the fire, leading to less time for particle evolution during transport. As the smoke blew in during the course of the data retrieval, the backscatter coefficient intensity is seen to increase in distance. This is contrasted with the extinction which stays roughly constant in intensity and height, as indicated by the drop in lidar ratio seen in Figure (30 b). The single profiles for backscatter and extinction coefficients indicate that the smoke was densest below 400 m, Figure (31).

Also shown in Figure (31) is the AOD which indicates a slightly higher density of smoke with an average of .18 compared to .16 on June 26th. The lapse rate was again found to be close to the accepted average at 7.4 K/km indicating a slightly dryer Troposphere. This and the calibration constant are shown in Figure (32).

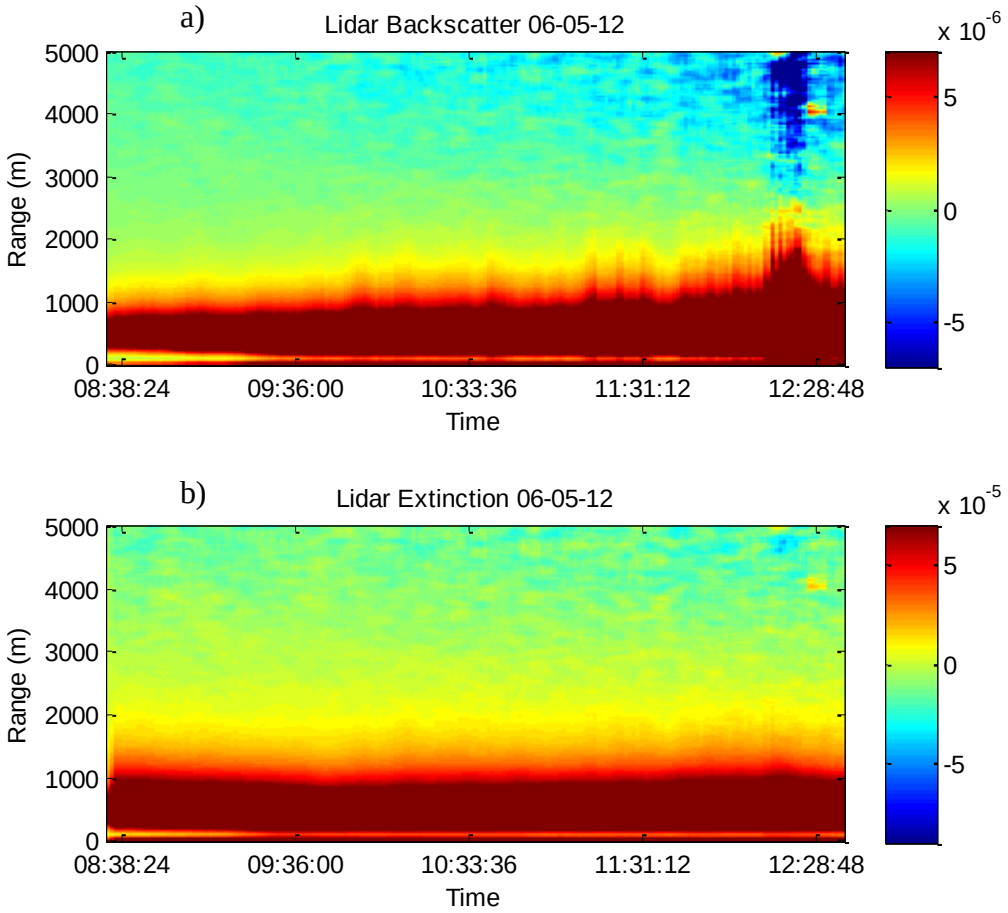


Figure (29) a) the retrieved aerosol backscatter profile in the boundary layer b) the retrieved aerosol extinction profile in the boundary layer.

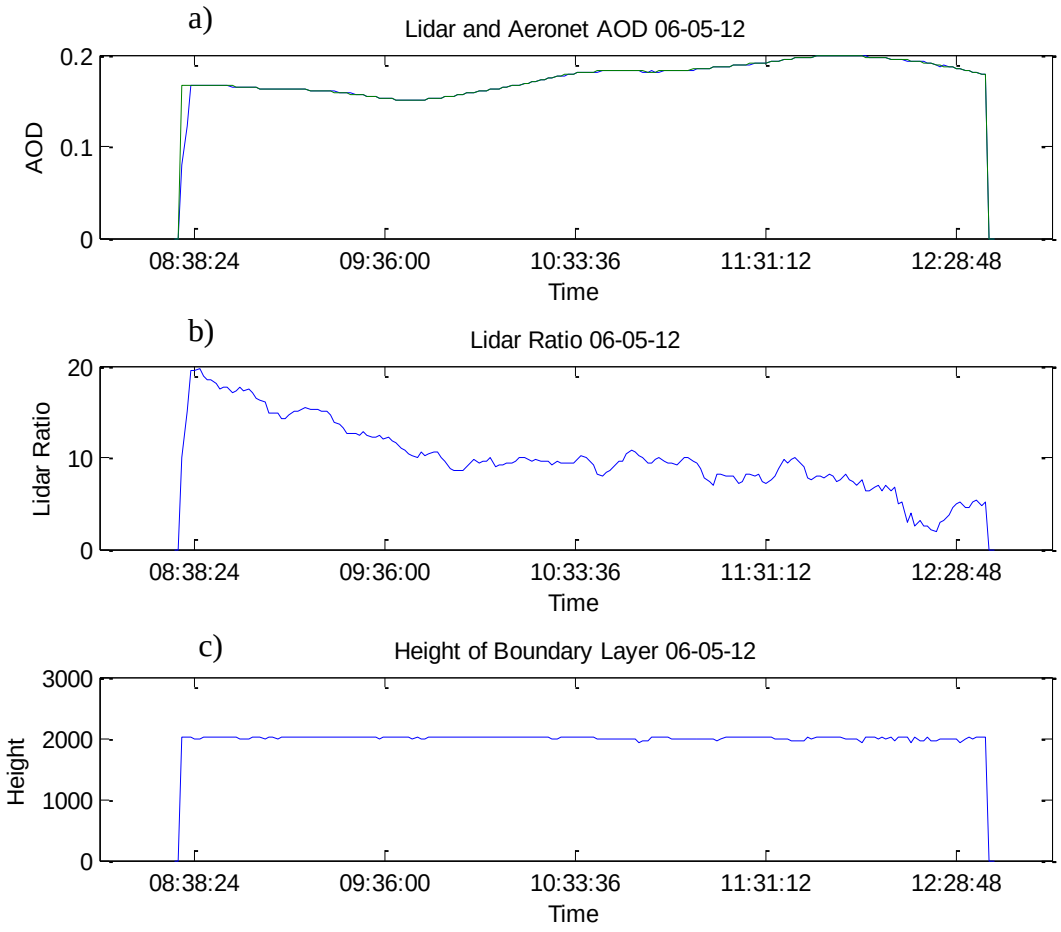


Figure (30) a) The AERONET AOD is plotted in green and the lidar retrieved AOD is plotted in blue. b) The lidar Ratio as a function of time. c) The boundary layer height as a function of time

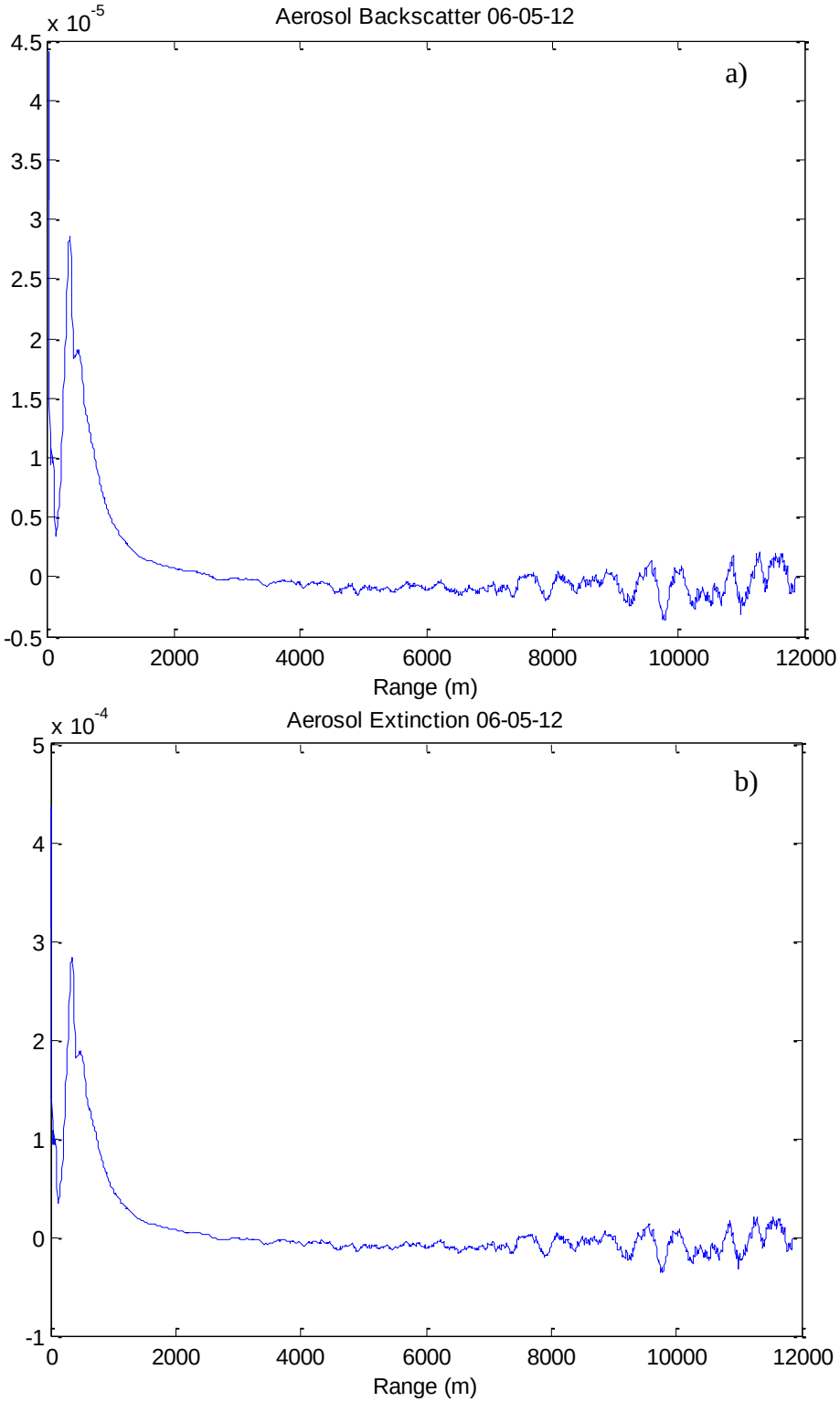


Figure (31) a) The aerosol backscatter coefficient as a function of range. b) The corresponding extinction coefficient as a function of range.

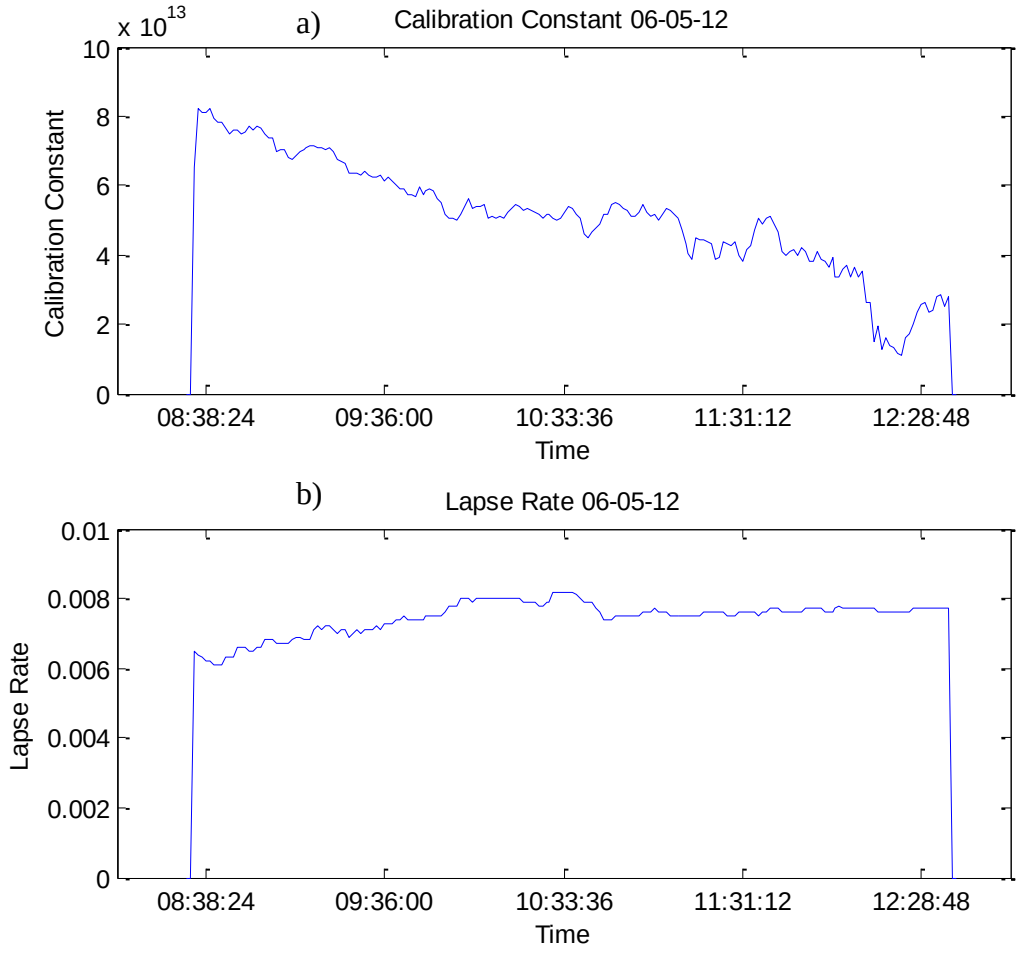


Figure (32) a) The calibration constant as a function of time. b) The lapse rate as a function of time.

June 7th 2012

A standard clean atmosphere, typical of Bozeman, Montana is presented; as it was detected on June 7th. As can be seen in the range corrected returns Figure (33) there were no apparent clouds and little evidence of aerosols until the cloud developing at 11:30 around 8 km. This is confirmed after the inversion by the aerosol backscatter and extinction as seen in Figure (34). The AOD was on average .06 as retrieved from transmission data by AERONET. The inverted MPL AOD is matched to this in Figure (35 a). The aerosol lidar ratio retrieved from the aerosol backscatter and extinction is shown in Figure (35 b) and seen to be roughly 70 sr for the data set indicative of a clean atmosphere as expected. The boundary layer is stable at 700 m for this retrieval.

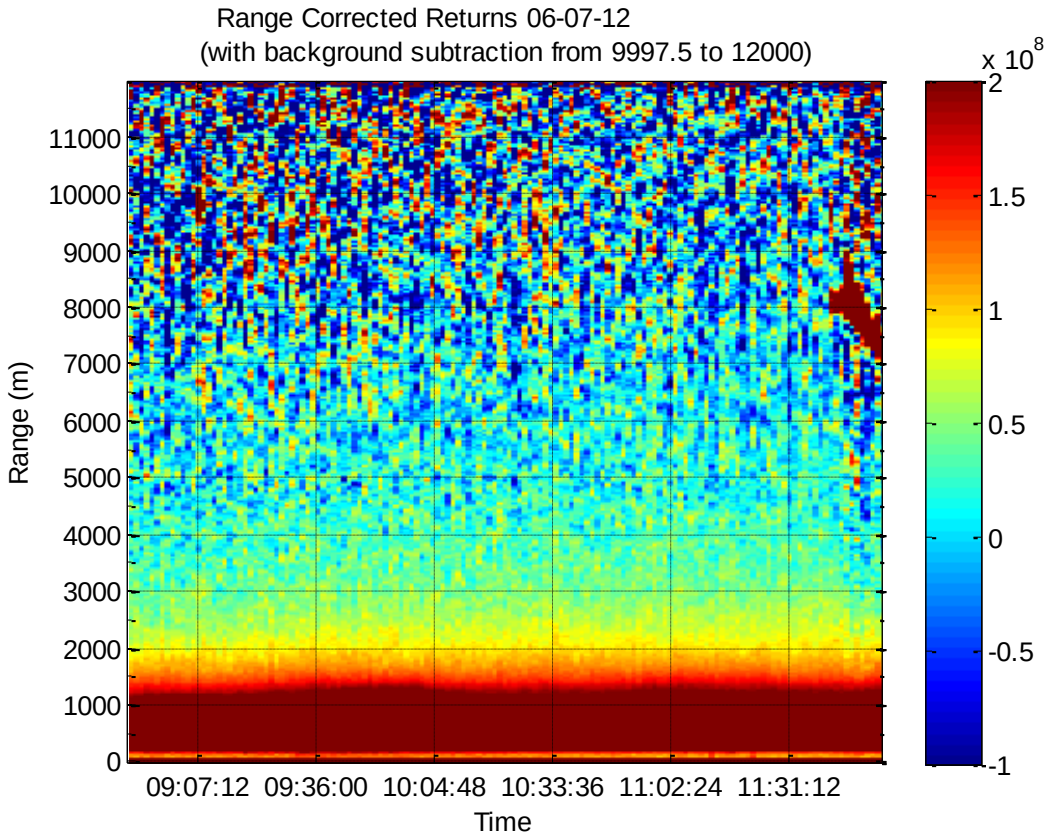


Figure (33) The range corrected returns for June 7th. Note the cloud developing around 11:30.

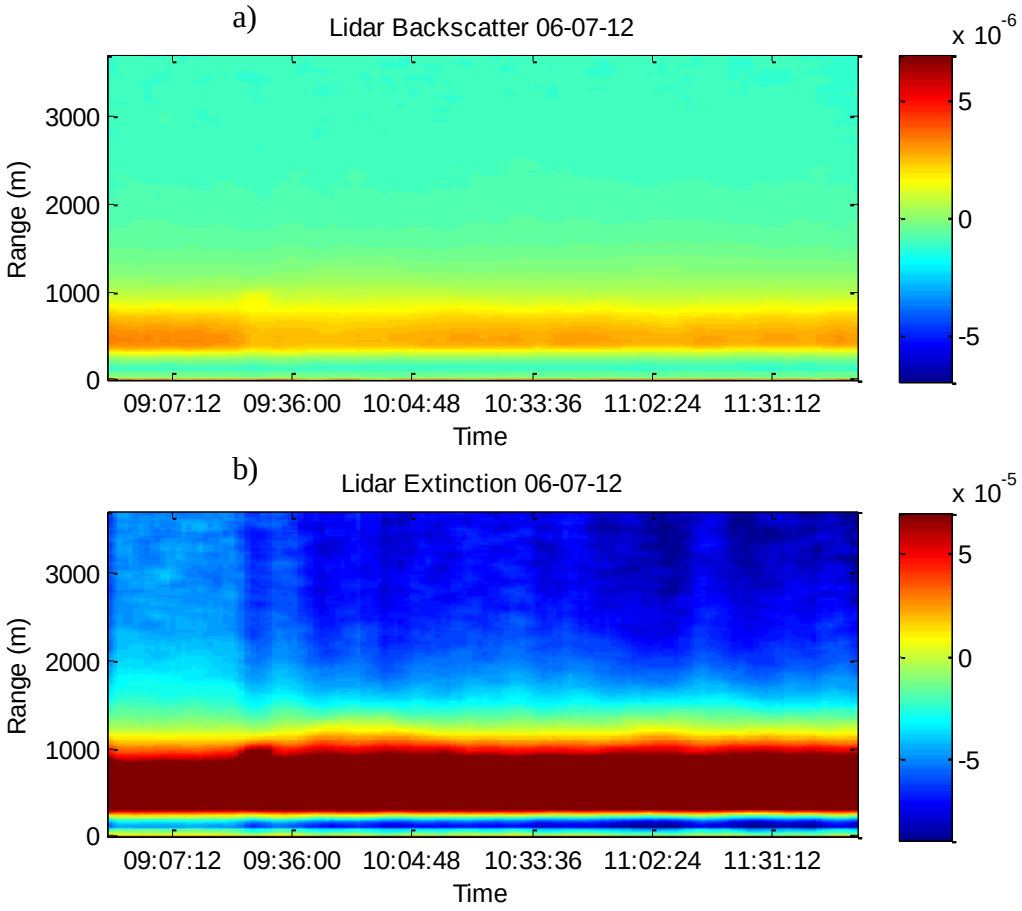


Figure (34) a) The aerosol backscatter coefficient. b) The aerosol extinction coefficient.

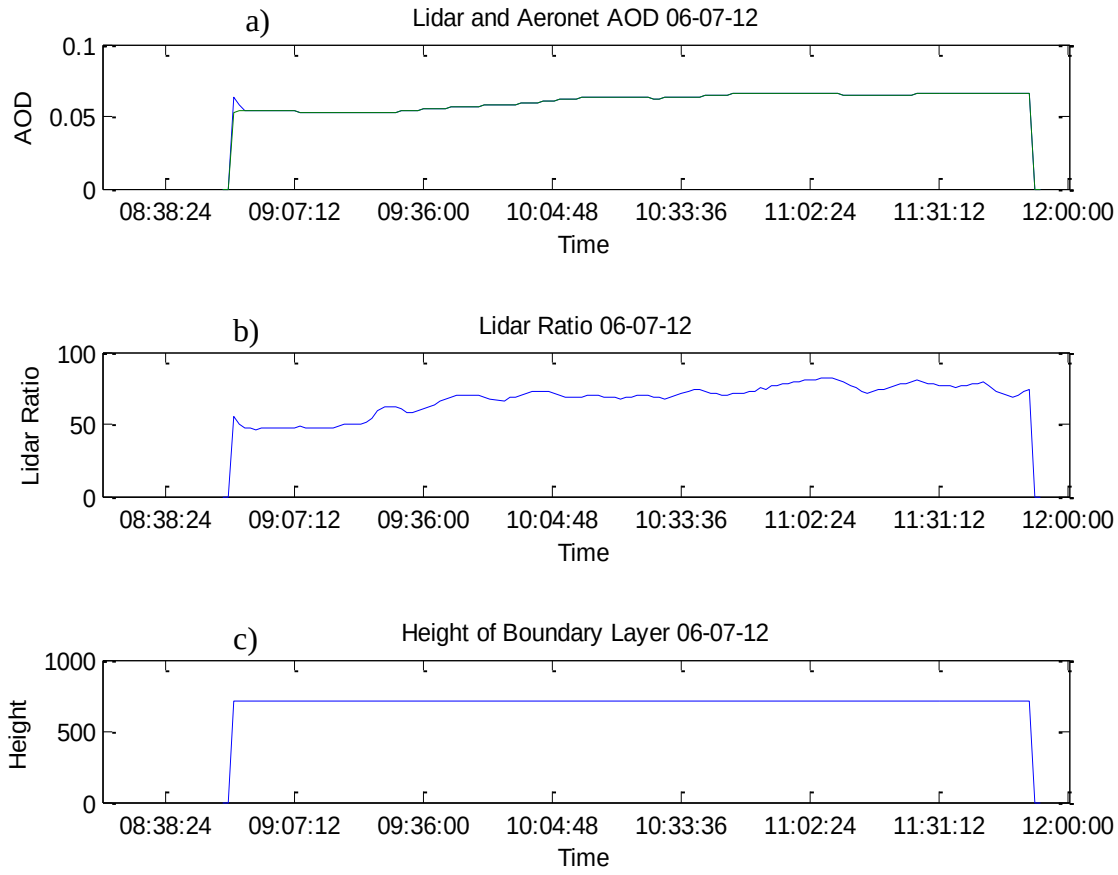


Figure (35) a) The AERONET AOD is plotted in green and the well matched MPL retrieved AOD is plotted in blue. b) The aerosol lidar ratio is roughly 70 sr for the entire data set. c) The boundary layer stays stable at 700 m for this data set.

The lapse rate found from the inversion of the returns on June 7$^{th}$ is shown in Figure (36 b). It is seen to sustain roughly the accepted average rate of 6.5 K/km for the whole data set. Also shown in Figure (36 a) is the calibration constant, presented to show that it is indeed a constant retrieved through the inversion method discussed previously.

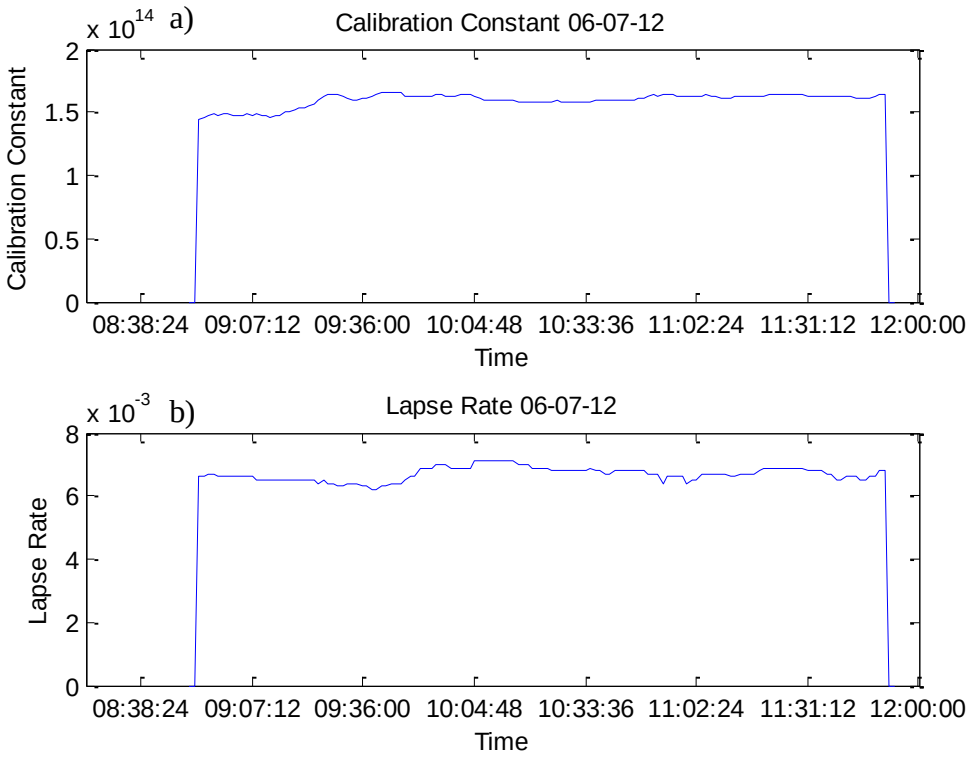


Figure (36) a) The calibration constant retrieved through the inversion. b) The lapse rate retrieved through the inversion is seen to be close to the accepted average.

March 10th 2012

The range corrected returns as presented in Figure (37), and seen initially on the Labview interface waterfall plot, seemed promising for study as they were not the clean troposphere of June 7th nor a smoke filled atmosphere seen on the 5th and 26th. Aside from the cloud that developed at 15:00 around 3.5 km this was a cloud free day making it ideal for aerosol studies. Also of note is the decay in intensity of the returns after 13:26 to and initial spike followed above 1 km by an increase in backscatter. These returns were of particular interest due to this unusual shape. As seen in Figure (38) the typical returns do not include a large initial spike. This unusual return shape was correlated with other instruments at Montana State University and verified.

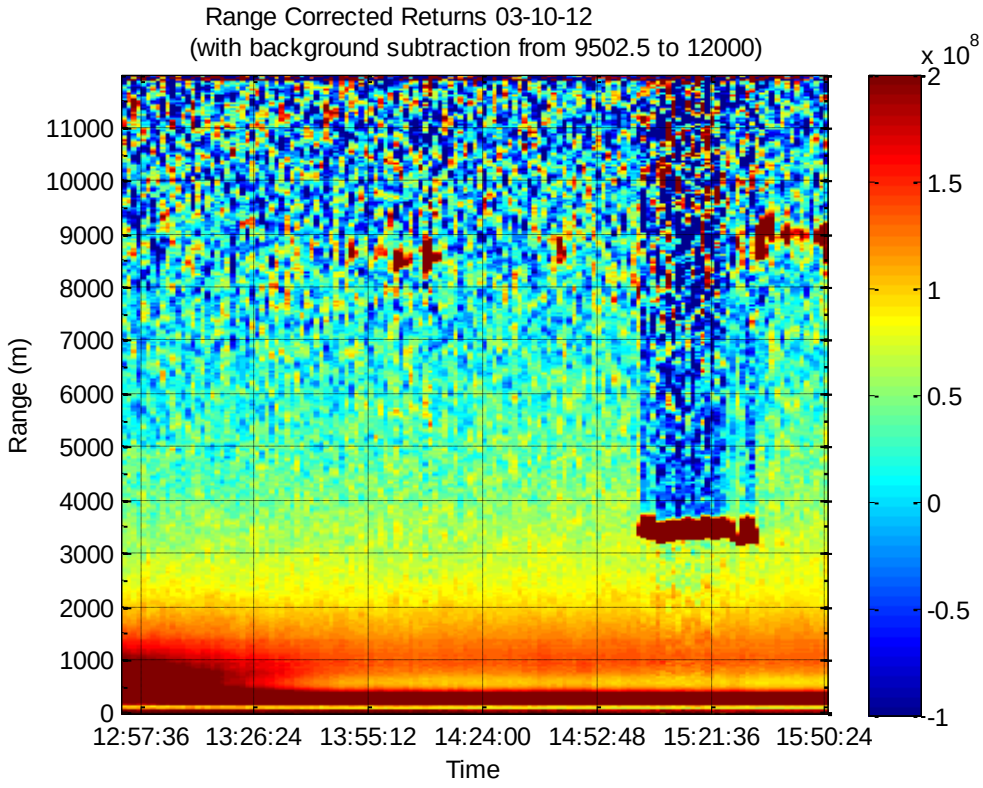


Figure (37) Range corrected return intensity plot as a function of time and range. The spike at 15:00 is a cloud and has been removed from the following data.

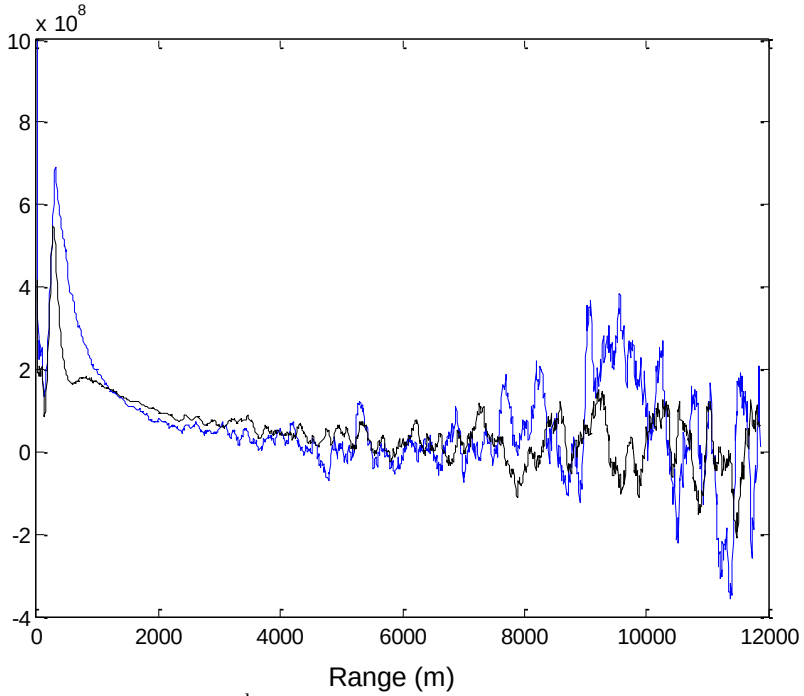


Figure (38) The March 10th return is plotted in black, compared to the average return plotted in blue. The blue is missing the sudden drop at 500 m.

After performing the inversion for the returns the backscatter and extinction profiles have been determined for the atmospheric aerosols. These are presented in Figure (39) as a false color plot for the entire data set. Presented in Figure (40) is a single profile for both the backscatter and extinction.

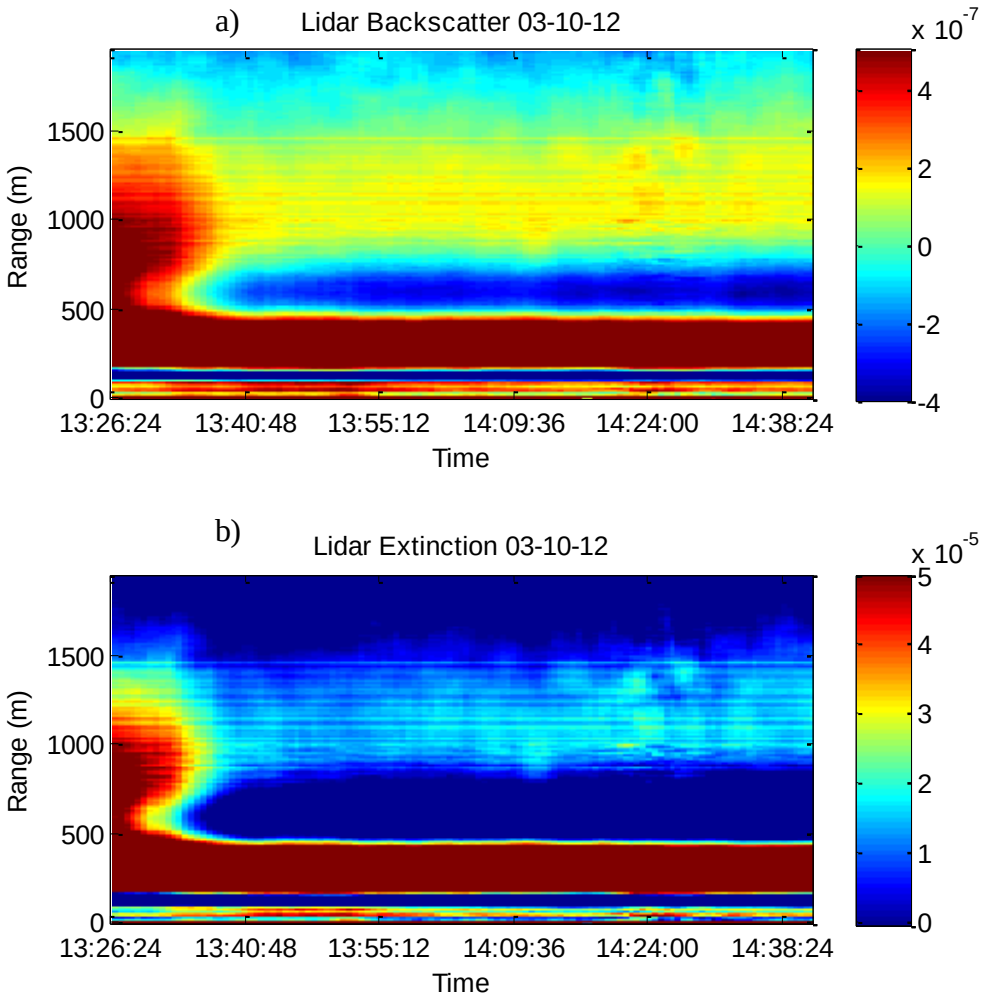


Figure (39) a) the retrieved aerosol backscatter profile in the boundary layer b) the retrieved aerosol extinction profile in the boundary layer.

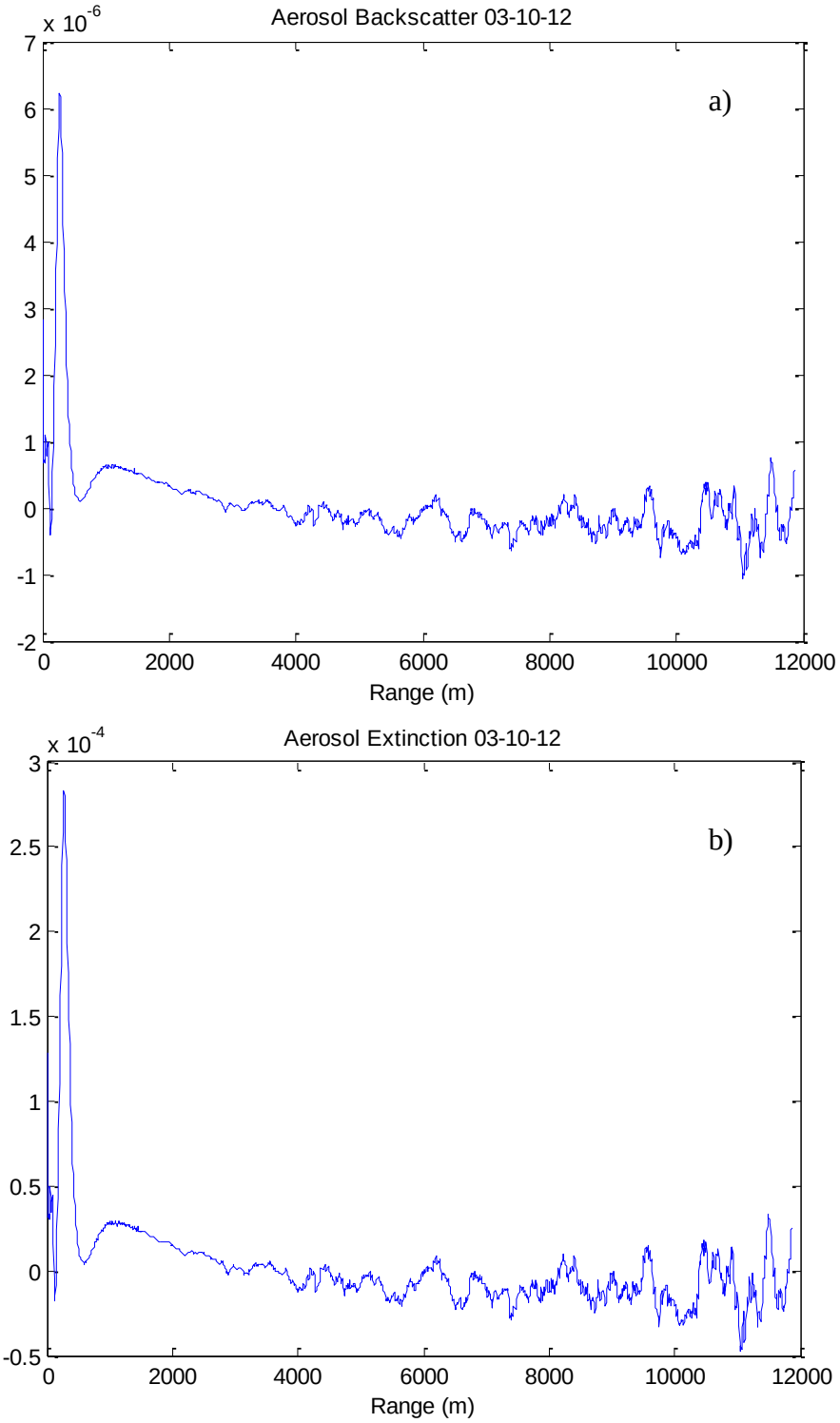


Figure (40) a) The aerosol backscatter coefficient as a function of range typical for the time after 13:40. b) The corresponding extinction coefficient as a function of range.

The aerosol optical depth found was roughly .08 after 13:55. As there was a dramatic change in the ABL before and after that point the AOD would be expected to change. As the AERONET instrument housed at Montana State University was undergoing repairs this data set was correlated with the High Spectral Resolution Lidar being developed here. As such there is only a single aerosol optical depth with which to correlate this data, that of .08. Both AOD's are plotted in Figure (41 a). The aerosol lidar ratio found for the 10$^{th}$ of March hovered around 100 sr for the entire data set. After the initial decay into the separated layers the lidar ratio has a positive trend as is shown in Figure (41 b). The height of the Boundary Layer as plotted against time shows the distinction between the two time periods as it rapidly decays from 1000 m and then maintains the value of 500 m as shown in Figure (41 c). This inversion was performed using the calibration constant as shown in Figure (42 a). As would be expected it is constant with a value of 10e13. The lapse rate found from this inversion was closer to the dry adiabatic lapse rate of 9.8 K/km than to the average 6.5 K/km seen on June 7$^{th}$. It started closer to the average and roughly at the time of the boundary layer separation it increased as is seen in Figure (42 b) indicating a low humidity.

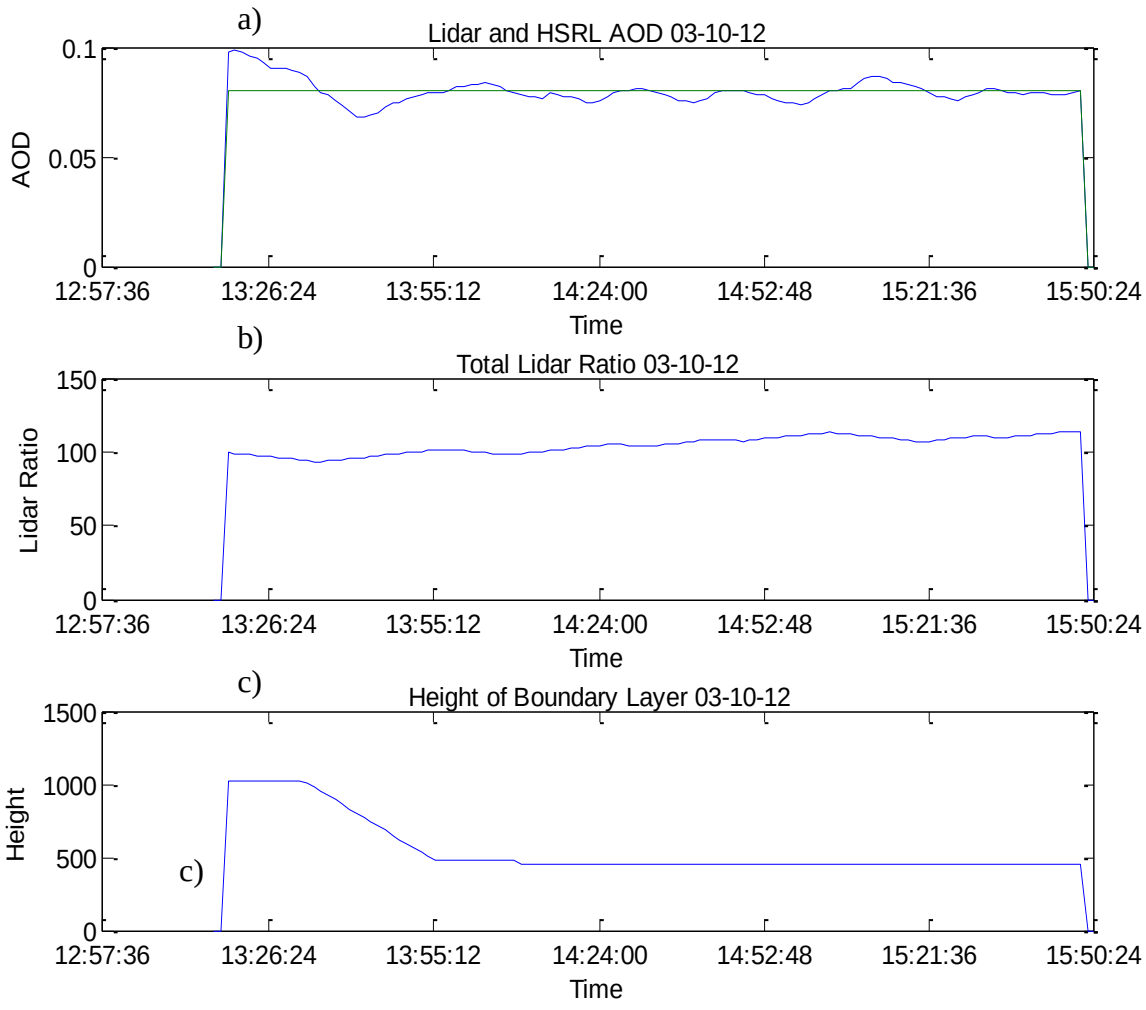


Figure (41) a) the AOD as found from the inversion of the MPL returns is plotted in blue, the reference AOD found from HSRL data is plotted in green. b) the lidar ratio $S_a$ as a function of time maintaining an average of 100 sr. c) the boundary layer height found as a function of time.

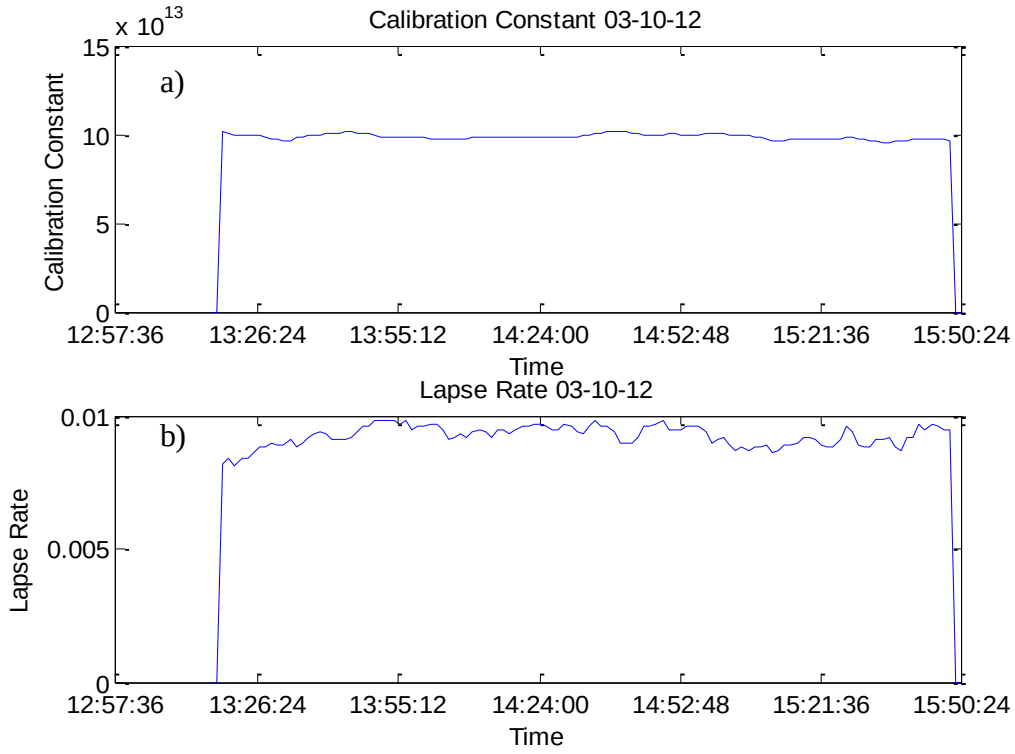


Figure (42) a) the calibration constant found for each return b) the lapse rate found iteratively for Gaussian noise matching of the slope.

# CHAPTER FIVE – CONCLUSIONS AND FUTURE WORK

## Conclusions

### Design and Fabrication

The micro-pulsed lidar instrument was successfully designed and built according to the theories presented, which specify the requirements of such a system. The MPL was further built for the purpose of continuous data collection and as such was designed to be eye-safe. This system has been incorporated into the set of instruments housed at Montana State University for the purpose of atmospheric studies. The MPL will contribute aerosol characterization information and aid specifically in lower tropospheric studies.

### Results

The results presented demonstrated the functionality of the optical system itself as well as the return acquisition software and the inversion programs. The returns from the 26$^{th}$ of June were correlated to Caliop data and verified with the lidar ratio of 40 sr. This is contrasted with a similar smoke filled atmosphere on the 5$^{th}$ of June which had a lidar ratio of 10 sr indicating a difference in transport of particles and varying radiative forcing due to smoke.

The returns of the MPL for the 7$^{th}$ of June show a clean atmosphere. This correlates to a lidar ratio of 70 sr and a lapse rate close to the accepted average. The boundary layer is seen to be at about 700 m with low intensity aerosol and backscatter coefficients retrieved below. As this is the most typical atmosphere for Bozeman,

Montana the set of instruments developed here are able to study the changes from a clean atmosphere to an aerosol filled one on the rare occasion of aerosols being introduced.

The returns gathered from the 10th of March indicate the utility of tracking aerosols with MPL data. Concurrently the ABL and lapse rate are monitored and correlated to the position and characterization of aerosols. This will allow for easy correlation with temperature and tropospheric changes. The increase of lapse rate on this day to being much closer to the dry adiabatic lapse rate, along with the separation of the ABL indicates much different chemistry from the other days presented.

The boundary layer itself is seen to increase from 500 m on March 10th to 2 or 2.5 km when smoke is present, both differing from the clean boundary layer of 700 m. Aside from the chemical changes inherent in the introduction of smoke the optical depth was doubled. All of which will influence radiative forcing models.

## Future Work

The MPL presented has potential to provide information about the troposphere above Bozeman, Montana. It will be run in conjunction with the set of in-situ and remote sensing instruments already in place at Montana State University. Incorporating this Lidar will allow for a more complete characterization of aerosols and the ABL and inform climatic conclusions based on this set of instruments.

Polarized versus un-polarized light can differentiate crystalline scatterers from non-crystalline. A polarization differentiation in the MPL returns would thus allow for cloud monitoring as well as aerosol monitoring. This addition would require an added

beam splitter in the receiver optics placed between the telescope focus and the fiber optic coupler currently in place. This would send polarized light to the current photodetector and rejected un-polarized light to a secondary fiber optic cable and photodetector. Both of these return signals then will be sent to the multi-channel scalar card. As the MCS is capable of multiple inputs, the only other addition would be creating a secondary channel in Labview running in sync with the first.

# REFERENCES

[1] US Standard Atmosphere (1976), Publication NOAA-S/T76-1562, Washington DC: US Government Printing Office.

[2] Stull, R. B., (1988), *An Introduction to Boundary Layer Meteorology.* Kluwer Academic Publishers.

[3] Yu, H. Y., et al. (2006), A review of measurement-based assessments of the aerosol direct radiative effect and forcing, Atmos. Chem. Phys., 6, 613–666.

[4] Rennick, M. A. (1977), The Parameterization of Tropospheric Lapse Rates in Terms of Surface Temperature. *J. Atmos. Sci.*, 34, 854–862.

[5] Wallace, J. M. and P. V. Hobbes (2006), *Atmospheric Sciences: An Introductory Survey*, Second Edition, Elsevier Inc.

[6] Morcrette, J. (2000), Radiation Transfer, http://www.ecmwf.int/newsevents/training/rcourse_notes/PARAMETRIZATION/RADIATION_TRANSFER/Radiation_transfer3.html

[7] Coakley, J. A., and P. Chylek (1975), The two-stream approximation in radiative transfer: Including the angle of the incident radiation, J. Atmos. Sci., 32, 409–418.

[8] Chylek, P., and J. Wong (1995), Effects of absorbing aerosols on global radiation budget, Geophys. Res. Lett., 22(8), 929–931.

[9] Haywood, J. M., and K. P. Shine (1995), The effect of anthropogenic sulfate and soot aerosol on the clear sky planetary radiation budget, Geophys. Res. Lett., 22(5), 603–606.

[10] Intergovernmental Panel on Climate Change (IPCC) (2007), *Climate Change 2007: The Scientific Basis. Contribution of Working Group I to the Fourth Assessment Report of the Intergovernmental Panel on Climate Change*, edited by S. Solomon et al., Cambridge Univ. Press, New York.

[11] Twomey, S. (1974), Pollution and the planetary albedo, Atmos. Environ., 8, 1251–1256.

[12] McComiskey, A., and G. Feingold (2008), Quantifying error in the radiative forcing of the first aerosol indirect effect, Geophys. Res. Lett., 35, L02810.

[13] Kovalev, A. K., and W. E. Eichinger (2004), *Elastic lidar*, John Wiley & Sons Publishers.

[14] Frick-Begemann, C. (2004), *Lidar Investigations of the Mesopause Region: Temperature Structure and Variability*. Doctoral Dissertation, University of Rostock.

[15] Fernald, F. G., B. M. Herman, and J. A. Reagan (1989), Determination of aerosol height distributions by lidar, J. Appl. Meteor., 77, 433-448.

[16] Nehrir, A. R. (2011), *Development of an eye-safe diode-laser-based micro-pulse differential absorption lidar (MP-DIAL) for atmospheric water-vapor and aerosol studies*. Doctoral Dissertation, Montana State University.

[17] Hoffman, D. S. (2008), *Two-wavelength lidar instrument for atmospheric aerosol study*, Master's Thesis, Montana State University.

[18] *NASA Langley Research Center Atmospheric Science Data Center.* http://eosweb.larc.nasa.gov/, 2012.

[19] Aeronet data download tool. http://aeronet.gsfc.nasa.gov/new_web/index.html

# APPENDICES

# APPENDIX A

## PROCEDURE FOR OPERATING MICRO-PULSE LIDAR

## Startup Procedure for MPL

1. Open the roof port.
2. Take the cover off of the telescope.
3. Turn the laser on with the key then use the laser start button to initialize lasing.
4. Turn on the triggering photodetector that is next to the laser.
5. Plug in the Avalanche Photo Diode detector that is on the bottom of the shelving unit.
6. Turn on the scalar card which is on the second shelf of the shelving unit.
7. Turn on the laptop and open run_micro_v10_3.vi as seen in Figure (6); which is located in:

   C:\Documents and Settings\Kevin Repasky\Desktop\microlidar\Labview
8. Press the run button in the upper left hand corner of the Labview program.
9. To stop the program press the global stop button once then the reset button.

## Alignment Procedure for MPL

1. Open run_micro_v3.vi
   a. Located in:

      C:\Documents and Settings\Kevin Repasky\Desktop\microlidar\Labview
   b. This older version does not save data and the plotting makes alignment clearer.
2. Follow all other steps in the above startup procedures.

3. Adjust only the transmitter optics; the mirrors on the top of the periscope and the lower mirrors in the z-fold.
4. The MPL will be aligned when the return signal is roughly 50 at 1.5 km and the overall shape is similar to that in Figure A-1.
5. If the receiving optics need to be adjusted to align the system the overlap function will need to be re-calculated using the procedure outlined in chapter three.

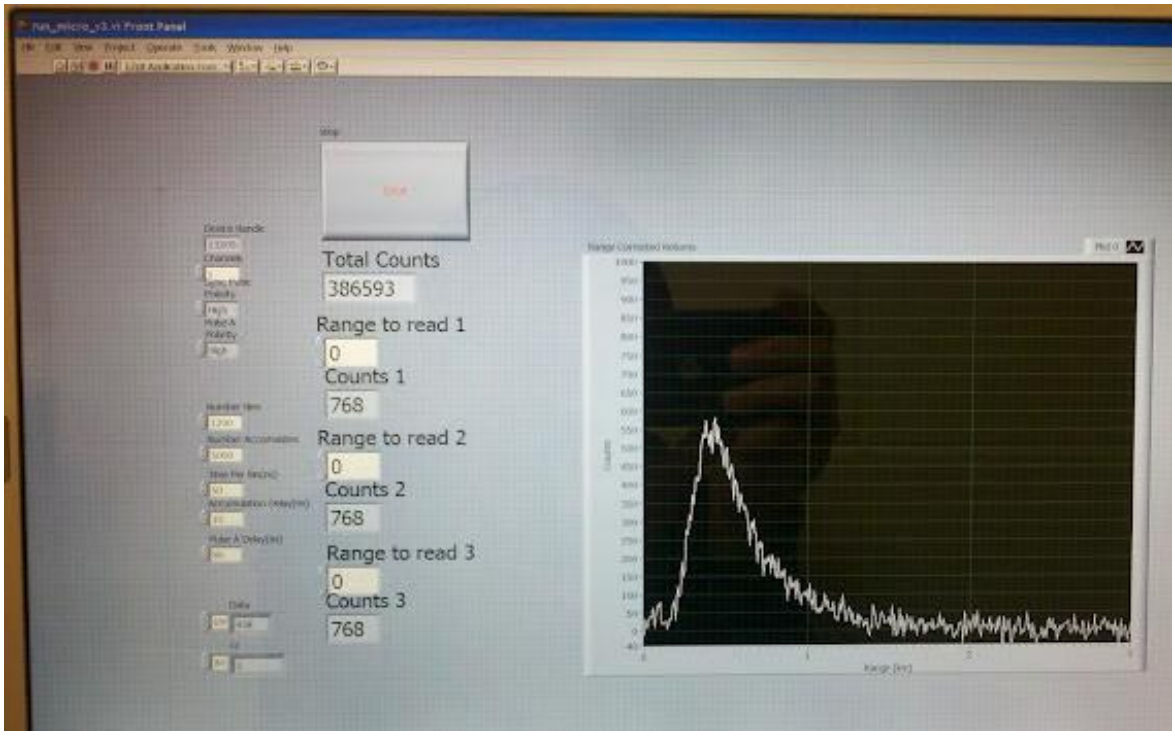


Figure A-1: The return signal for a fairly well aligned system.

Error Codes in Labview Scalar Card Returns

1. Scalar card return value of -1 instead of 0 implies the photodetector trigger is out of battery power or misaligned.

2. Scalar card return value of -3 instead of 0 implies there is something wrong with the return, usually just restarting the whole system will fix this.
3. If the data is returned but all values are “0” the APD likely overheated and needs to be unplugged briefly. This happens on really cloudy days with high photon counts and when the APD has been moved off of the heat sink.

# APPENDIX B

## PROCEDURE FOR OPERATING INVERSION

Inversion Procedure

1. Three files are needed for the inversion
    a. Return data should be located in:

       C:\Users\erin.casey2\Desktop\microlidar\Data\mon\mm-dd-yy\data

       Where mon is the three letter abbreviation for month, mm, dd and yy the numerical month, day, and year of the return data.
    b. Weather station data
        i. Download from: http://orsl.eps.montana.edu/weather/
        ii. Move file to:

            C:\Users\erin.casey2\Desktop\microlidar\Data\mon\mm-dd-yy
    c. AERONET data
        i. Download from: http://aeronet.gsfc.nasa.gov/cgi-bin/webtool_opera_v2_new?stage=3&region=United_States_West&state=Montana&site=Bozeman&place_code=10
        ii. Move zip-file to:

            C:\Users\erin.casey2\Desktop\microlidar\Data\mon\mm-dd-yy
        iii. Extract data into same folder
2. Matlab can now run the inversion program, mpl_inversion, with the following inputs located at the top of the code:
    a. Date
    b. Month
    c. Approximate lidar ratio

d. Approximate ABL height

e. Background subtraction range

# APPENDIX C

## MATLAB INVERSION CODE

```
% Program to invert micro-pulse lidar returns

%% Input parameters

date = '06-07-12';

month = 'Jun\';

%these two change in loops to find right one

lidar_ratio = 60;

lapse = .0065;                %K/m

bottomlim = round(500/7.5);

toplim = round(700/7.5);

aeronet = 1;         %did you download aeronet data? yes=1


%variable limits

aodlim = round(500/7.5);

back1=round(10000/7.5);       %avoid clouds

back2=round(12000/7.5);


%data will also be saved to this file

filepath = 'C:\Users\erin.casey2\Desktop\microlidar\Data\';

filename = ['\' date ];

path = dir([filepath month date '\data']);

s = size(path);

L1(s,1) = struct( 'data', [], 'textdata', [],

'colheaders',[]);
```

```
O = importdata('C:\Users\erin.casey2\Desktop\microlidar\
     Overlap Function\O.mat');


%% This cell imports and concatenates the data and times
for n = 3:(s(1));
    L1(n,:) = importdata([filepath month date '\data\'
          path(n,1).name]);
    Time1 = datenum(L1(n,1).textdata, 'dd-mmm-yy
          HH:MM:SS');
%concatenates data if less than 10 minute gap, each point
           is 68.5 sec long
        if n >= 4
            t1 = Time(size(Time,1),1);
            if Time1(1,1) > t1+.0069
                tn = t1:8.1019e-4:Time1(1,1);
                Ln = single(zeros(size(tn,2),1600));
                Time = cat(1, Time, tn');
                L = cat(2, L, Ln');
                    %then add data
                Time = cat(1, Time, Time1);
                L = cat(2, L, L1(n,1).data);
            else
                L = cat(2, L, L1(n,1).data);
```

```
                Time = cat(1, Time, Time1);
            end
        else
            L = L1(n,1).data;
            Time = Time1;
        end

end

%% This cell Pre-allocates space
L = transpose(L(:,255:400));
t = size(L,1);              %time dimension
d = size(L,2);              %distance dimension
r = (0:7.5:d*7.5-1);        %range vector
Time = Time(1:t);           %pulling out times for actual run

%% This cell subtracts background, range corrects, and
range averages
for n = 1:t;
    L(n,:) = (L(n,:)-mean(L(n,back1:back2))).*(r.^2);
    for m = 2:135
        L(n,m) = mean(L(n,m-1:m+1));
    end
```

```
    for m = 136:700    %75m rangebins
        L(n,m) = mean(L(n,m-10:m+10));
    end
    for m = 701:d-16   %112m rangebins
        L(n,m) = mean(L(n,m-15:m+15));
    end
L(n,:) = L(n,:)./O;    %correcting for the overlap function.
end

%% This cell plots the range corrected returns.
figure (101)
imagesc(Time,r,L',[-1e8 2e8]);
set(gca,'YDir', 'normal', 'YTick', 0:1000:12000,
     'YMinorTick', 'on')
datetick('x','HH:MM:SS', 'keeplimits', 'keepticks')
xlabel('Time');
ylabel('Range (m)');
title(['Range Corrected Returns ' date ,sprintf('\n'),  '
     (with background subtraction from ' num2str(back1*7.5)
     ' to ' num2str(back2*7.5) ')']);
colorbar;
grid on
saveas(gcf,[filepath month date '\' date
```

```
    '_range_corrected_returns.fig'])
saveas(gcf,[filepath month date '\' date
    '_range_corrected_returns.jpg'])

%% This cell finds the rest of the inputs for the inversion
%Input Parmaters that don't change
dr = 7.5;          %rangebin size in m
Sm = 8*pi/3;       %Lidar Ratio for Rayleigh Scattering in sr
Sa = lidar_ratio;
avg = 2;           %2 ~6min averaging
%deleting noisy (un-averaged) sections
L = L(1:t,2:d-16);
Time = Time(1:t);          %pulling out times for actual run

%Pre allocating space
t = size(L,1);             %resize
d = size(L,2);             %resize
r = (0:7.5:d*7.5-1);       %resize
Lidar_extinction = single(zeros(t,d));
Lidar_backscatter = single(zeros(t,d));
Lidar_AOD = single(zeros(t,1));
Lidar_Ratio = single(zeros(t,1));
Lapse_Rate = single(zeros(t,1));
```

```
Cimel_AOD = single(zeros(t,1));
Calibration_Constant = (zeros(t,1));
Boundary_layer = (zeros(t,1));
Boundary_layer2 = (zeros(t,1));

%% This cell finds the right times and imports the
temperature and pressure
for n=1:1
 % This rounds the start time and end time to the nearest 5
         minute interval
    startmin = round((str2double(datestr(Time(1),
          'MM')))/5)*5;
    endmin = round((str2double(datestr(Time(t),
          'MM')))/5)*5;
        if startmin <= 55 && endmin <= 55
            start_time = ([datestr(Time(1),'HH')
               ':'num2str(startmin)]);
            end_time = ([ datestr(Time(t), 'HH') ':'
               num2str(endmin)]);
        else
            if startmin <= 55

start_time=([datestr(Time(1),'HH')':'num2str(startmin)]);
```

```
            else
                start_time = ([num2str(str2double
                    (datestr(Time(1),'HH')) +1) ':' '00']);
            end
            if endmin <= 55
                end_time = ([ datestr(Time(t), 'HH') ':'
                    num2str(endmin)]);
            else
                end_time = ([num2str(str2double
                    (datestr(Time(t),'HH')) +1) ':' '00']);
            end
        end

%Importing weather station temperature and pressure for
correct times.
    X1=round(1000*(xlsread([filepath month date '\'datestr
     (datenum(filename), 'mmddyyyy')'.csv'],'B2:B289')));
    X2=round(1000*(datenum(start_time, 'HH:MM')-
     datenum(datestr(Time(1), 'yyyy'), 'yyyy')));
    ind1=find(X1==X2);
    X3=round(1000*(datenum(end_time, 'HH:MM')-datenum
     (datestr(Time(t),'yyyy'), 'yyyy')));
    ind2=find(X1==X3);
```

```
    P0 = xlsread([filepath month date '\' datestr(datenum
     (filename),'mmddyyyy') '.csv'],['D' num2str(ind1) ':D'
     num2str(ind2)]);
    P0 = interp(P0,ceil(t/(ind2-ind1)));
    P0 = P0(1:t);              %inHg
    T0 = xlsread([filepath month date '\' datestr(datenum
     (filename),'mmddyyyy') '.csv'],['G' num2str(ind1) ':G'
     num2str(ind2)]);
    T0 = interp(T0,ceil(t/(ind2-ind1)));
    T0 = T0(1:t)+273.15;       %kelvin
end
%% this cell imports the aeronet data.
for n = 1:1
    if aeronet == 1

    path01 = dir([filepath month date '\'datestr(datenum
     (filename),'yymmdd') '_' datestr(datenum(filename),
     'yymmdd') '_Bozeman']);
    aod_aeronet1 = importdata([filepath month date '\'
     datestr(datenum(filename), 'yymmdd') '_'
     datestr(datenum(filename), 'yymmdd') '_Bozeman' '\'
     path01(3).name], ',',5);
```

```
aod_aeronet2 = aod_aeronet1.textdata;


% % reads in the aeronet times
aodtime = round(1000*(datenum(aod_aeronet2(6:size(
 aod_aeronet2,1),2))-datenum(datestr(datenum(
 aod_aeronet2(6,2)), 'yyyy'),'yyyy')-.25));
% % finds the start and end time of the data captured
starttime01 = round(1000*(datenum(datestr(Time(1),
 'HH:MM:SS'))- datenum(datestr(Time(1), 'yyyy'),
 'yyyy')));
endtime01 = round(1000*(datenum(datestr(Time(t),
 'HH:MM:SS'))- datenum(datestr(Time(t), 'yyyy'),
 'yyyy')));
% % matching times
ind02 = 0;
for n01 = 1:size(aodtime,1)
    if (starttime01 < aodtime(n01)) && (aodtime(n01) <
      endtime01)
    ind02 = n01;
    ind01(n01) = n01;
    end
end
ind011 = find(ind01,1,'first');
```

```
    aod_aeronet =str2double(aod_aeronet2(ind011:ind02,13));
    aod_aeronet = interp(aod_aeronet,ceil(t/size(
     aod_aeronet,1)));
    aod_aeronet = aod_aeronet(1:t);
    aod_ave = aod_aeronet;

    else
    aod_ave = zeros(1,t);    %use for just 1 aod data point
    aod_ave(:) = aod;
    end
end

tic
        %% This cell does the INVERSION.
        for u = avg+1:t-avg;
            %loop for lapse rate and boundary layer
            for m = 1:5
                L_new = mean(L(u-avg:u+avg,:));
             %Loop to step through Sa's to get correct AOD
                    for ii = 1:100
                        % Defining Rayleigh atmosphere
                        T = T0(u)-lapse.*r;
```

```
P = P0(u).*3.386.*(T0(u)./T).^(-
.034164./lapse); %Pressure Profile
in kilopascals
bm = 374280.*P./(532.^4.*T);
%Rayleigh Backscatter Profile
(1/m*sr)

lim2 = aodlim + 200;
lim1 = aodlim;
Tm = exp(cumtrapz(-2.* Sm .*
bm.*dr,2));
%Rayleigh Transmission from ground up to max alititude
am = cumtrapz( bm .*dr,2);
CPt = L_new./( bm .*exp(-2* Sm .*
am).*exp(-2*
mean(aod_ave(u-avg:u+avg))));

%Calculating Calibration Constant as a function of range
CPt = mean(CPt(lim1:lim2));
%inversion integrations
gm = (L_new ./ Tm ) .*exp(-2.* Sa
.* am);
```

```
                    gm = cumtrapz( gm .*dr,2);

                    bt = L_new.*exp(-2*(Sa - Sm).*
                     am)./(CPt-2* Sa .* gm);

%forcing backscatter to fit Rayleigh between limitsmin and
limitsmax
                    if mean(bt(lim1:lim2)) >
                     mean(bm(lim1:lim2))
                        bt = bt -(mean( bt(lim1:lim2))
                          - mean(bm(lim1:lim2)));
                    else
                        bt = bt +(mean( bm(lim1:lim2))
                          -mean( bt(lim1:lim2)));
                    end

                    ba = bt - bm;  %aerosol backscatter
                    siga = ba .* Sa;%aerosol extinction
                    AOD = cumtrapz( siga .*dr,2);
                %% Finding the ABL
                [min_difference, array_position] =
                  min(abs(ba(bottomlim:toplim) - 0));
                aodlim = array_position+bottomlim;
```

```
%In case no data exists, make AOD = 0 and not NAN!
                        if L(u,200)== 0
                            AOD(:) = 0;
                        end
%AOD integrated up to the desired bin
                        AOD_final = AOD(aodlim);
                        %bounds on AOD
                        if isnan(AOD_final)
                            AOD_final = 0;
                        elseif AOD_final < 0
                            AOD_final = 0;
                        elseif AOD_final > 2*aod
                            AOD_final = 2*aod;
                        end

% Adding or subtracting from the Sa to get correct AOD
                        if AOD_final > 1*(mean(aod_ave(u-
                         avg:u+avg)))
                            Sa = Sa-.01;
                        elseif AOD_final < 1*(mean(aod_ave(
                         u- avg:u+avg)))
                            Sa = Sa+.01;
                        end
```

```
                %Max and min. bounds on the Sa
                if Sa > 200;
                    Sa = 200;
                elseif Sa < 0
                    Sa = 0;
                end
            end

%If there is no data, set beta and sigma = 0 and not NAN!
            if L(u,200) == 0
                siga(:) = 0;
                bt(:) = 0;
            end
            %inputs to find lapse rate fit
            l = lim2-lim1+1;
            b_match = double( bt(lim1:lim2));
            dif(1:l) = b_match(1:l) - bm(lim1:lim2);
            md = mean(dif);
            standiv = (sum((dif-md).^2)./(l-1)).^(1/2);
            ztest = (md-0)/(standiv/(l)^(1/2));

                if ztest > 2e-14
                    lapse = lapse -.0001;
```

```
            elseif ztest < -2e-14
                lapse = lapse +.0001;
            end

            %bounds on lapse rate
            if lapse > .0098
                lapse = .0098;
            elseif lapse < .004
                lapse = .004;
            end
        end


        Lidar_extinction(u,:) = single(siga);
        Lidar_backscatter(u,:) = single(ba);
        Lidar_Ratio(u) = Sa;
        Calibration_Constant(u) = CPt;
        Lidar_AOD(u) = AOD_final;
        Cimel_AOD(u) = mean(aod_ave(u-avg:u+avg));
        Lapse_Rate(u) = lapse;
        Boundary_layer(u) = aodlim;
    end
    toc
```

```
%%     This section plots backscatter and extinction.
    plotlim = lim2+200;
    figure (105)
    subplot(2,1,1)
    imagesc(Time(avg:(t-avg)),(.0075 :.0075:round(plotlim*
     7.5)),Lidar_backscatter(avg+1:t-avg,1:plotlim)',[-7e-6
     7e-6]);
    set(gca,'YDir', 'normal')
    datetick('x','HH:MM:SS', 'keeplimits', 'keepticks')
    xlabel('Time');
    ylabel('Range (m)');
    title(['Lidar Backscatter ' date ]);
    colorbar;


    subplot(2,1,2)
    imagesc(Time(avg:(t-avg)),(.0075 :.0075:round(plotlim*
     7.5)),Lidar_extinction(avg+1:t-avg,1:plotlim)',[-9e-5
     7e-5]);
    set(gca,'YDir', 'normal')
    datetick('x','HH:MM:SS', 'keeplimits', 'keepticks')
    xlabel('Time');
    ylabel('Range (m)');
    title(['Lidar Extinction ' date ]);
```

```
colorbar;
saveas(gcf,[ filepath month date '\' date 'Backscatter
 and Extinction.fig'])

%% This section plots AOD, Lapse Rate and Lidar Ratio
figure(106)
subplot(3,1,1)
plot (Time, Lidar_AOD(:), Time,Cimel_AOD)
set(gca,'YDir', 'normal')
datetick('x','HH:MM:SS', 'keeplimits', 'keepticks')
xlabel('Time');
ylabel('AOD');
legend('Lidar AOD','Aeronet AOD')
title(['Lidar and Aeronet AOD ' date]);

subplot(3,1,2)
plot (Time, Lidar_Ratio)
set(gca,'YDir', 'normal')
datetick('x','HH:MM:SS', 'keeplimits', 'keepticks')
xlabel('Time');
ylabel('Lidar Ratio');
title(['Lidar Ratio ' date]);
```

```
    subplot(3,1,3)
    plot (Time, Boundary_layer.*7.5)
    set(gca,'YDir', 'normal')
    datetick('x','HH:MM:SS', 'keeplimits', 'keepticks')
    xlabel('Time');
    ylabel('Hieght');
    title(['Hieght of Boundary Layer ' date]);
    saveas(gcf,[ filepath month date '\' date 'Lidar ratio
     and AOD and boundary layer.fig'])

%% Plotting lapse rate and calibration
    figure(107)
    subplot(2,1,2)
    plot (Time, Lapse_Rate)
    set(gca,'YDir', 'normal')
    datetick('x','HH:MM:SS', 'keeplimits', 'keepticks')
    xlabel('Time');
    ylabel('Lapse Rate');
    title(['Lapse Rate ' date]);

    subplot(2,1,1)
    plot (Time, Calibration_Constant)
    set(gca,'YDir', 'normal')
```

```
datetick('x','HH:MM:SS', 'keeplimits', 'keepticks')
xlabel('Time');
ylabel('Calibration Constant');
title(['Calibration Constant ' date]);
saveas(gcf,[ filepath month date '\' date 'Lapse rate
 and calibration constant.fig'])

save([filepath month date '\' date '.mat_2']);
```